



**NAVAL
POSTGRADUATE
SCHOOL**

MONTEREY, CALIFORNIA

THESIS

**HIGH ENERGY LASER (HEL) EFFECTIVENESS IN
THE MEDITERRANEAN MARITIME ENVIRONMENT**

by

Yusuf Temur

September 2024

Thesis Advisor:
Co-Advisor:

Keith R. Cohn
Joseph A. Blau

Distribution Statement A. Approved for public release: Distribution is unlimited.

THIS PAGE INTENTIONALLY LEFT BLANK

REPORT DOCUMENTATION PAGE			Form Approved OMB No. 0704-0188
<p>Public reporting burden for this collection of information is estimated to average 1 hour per response, including the time for reviewing instruction, searching existing data sources, gathering and maintaining the data needed, and completing and reviewing the collection of information. Send comments regarding this burden estimate or any other aspect of this collection of information, including suggestions for reducing this burden, to Washington headquarters Services, Directorate for Information Operations and Reports, 1215 Jefferson Davis Highway, Suite 1204, Arlington, VA 22202-4302, and to the Office of Management and Budget, Paperwork Reduction Project (0704-0188) Washington, DC 20503.</p>			
1. AGENCY USE ONLY (Leave blank)	2. REPORT DATE September 2024	3. REPORT TYPE AND DATES COVERED Master's thesis	
4. TITLE AND SUBTITLE HIGH ENERGY LASER (HEL) EFFECTIVENESS IN THE MEDITERRANEAN MARITIME ENVIRONMENT		5. FUNDING NUMBERS	
6. AUTHOR(S) Yusuf Temur			
7. PERFORMING ORGANIZATION NAME(S) AND ADDRESS(ES) Naval Postgraduate School Monterey, CA 93943-5000		8. PERFORMING ORGANIZATION REPORT NUMBER	
9. SPONSORING / MONITORING AGENCY NAME(S) AND ADDRESS(ES) N/A		10. SPONSORING / MONITORING AGENCY REPORT NUMBER	
11. SUPPLEMENTARY NOTES The views expressed in this thesis are those of the author and do not reflect the official policy or position of the Department of Defense or the U.S. Government.			
12a. DISTRIBUTION / AVAILABILITY STATEMENT Distribution Statement A. Approved for public release: Distribution is unlimited.		12b. DISTRIBUTION CODE A	
13. ABSTRACT (maximum 200 words) This thesis investigated the effectiveness of High Energy Lasers (HEL) in the Mediterranean maritime environment. The main focus was the influence of various atmospheric conditions on laser performance under different engagement scenarios. Numerical models, including the Scaling Law Model (SLM) and the Fresnel Diffraction Model (FDM), were employed to simulate laser beam propagation and predict the irradiance and the spot size at the target. Melt-through times for different target materials, including surface and aerial targets, were predicted using Torvik's model. The results revealed that both target material properties and atmospheric conditions play a significant role in the effectiveness of HELs. This research provides valuable insights into the operational limits and potential of HELs in the Mediterranean maritime environment.			
14. SUBJECT TERMS High energy laser, Mediterranean Sea, Atmospheric propagation, Effectiveness, Scaling law models, Fresnel Diffraction models, Melt-through time			15. NUMBER OF PAGES 95
16. PRICE CODE			
17. SECURITY CLASSIFICATION OF REPORT Unclassified	18. SECURITY CLASSIFICATION OF THIS PAGE Unclassified	19. SECURITY CLASSIFICATION OF ABSTRACT Unclassified	20. LIMITATION OF ABSTRACT UU

THIS PAGE INTENTIONALLY LEFT BLANK

Distribution Statement A. Approved for public release: Distribution is unlimited.

**HIGH ENERGY LASER (HEL) EFFECTIVENESS IN THE MEDITERRANEAN
MARITIME ENVIRONMENT**

Yusuf Temur
Lieutenant, Turkish Naval Forces
BSIE, Turkish Naval Academy, 2015

Submitted in partial fulfillment of the
requirements for the degree of

MASTER OF SCIENCE IN APPLIED PHYSICS

from the

NAVAL POSTGRADUATE SCHOOL
September 2024

Approved by: Keith R. Cohn
Advisor

Joseph A. Blau
Co-Advisor

Frank A. Narducci
Chair, Department of Physics

THIS PAGE INTENTIONALLY LEFT BLANK

ABSTRACT

This thesis investigated the effectiveness of High Energy Lasers (HEL) in the Mediterranean maritime environment. The main focus was the influence of various atmospheric conditions on laser performance under different engagement scenarios. Numerical models, including the Scaling Law Model (SLM) and the Fresnel Diffraction Model (FDM), were employed to simulate laser beam propagation and predict the irradiance and the spot size at the target. Melt-through times for different target materials, including surface and aerial targets, were predicted using Torvik's model. The results revealed that both target material properties and atmospheric conditions play a significant role in the effectiveness of HELs. This research provides valuable insights into the operational limits and potential of HELs in the Mediterranean maritime environment.

THIS PAGE INTENTIONALLY LEFT BLANK

Table of Contents

1	Introduction	1
1.1	Overview of High Energy Lasers	2
1.2	Thesis Structure and Overview	5
2	Propagation Physics	7
2.1	Properties of Laser Light	7
2.2	Atmospheric Effects on Laser Propagation	9
3	Numerical Models	17
3.1	Scaling Law Model	17
3.2	Fresnel Diffraction Model	19
3.3	Modeling of a Turbulent Atmosphere	27
3.4	Model Validation	29
4	Lethality Physics	31
4.1	Laser Interaction with Materials	31
4.2	Torvik's Model for Predicting Melt-Through Times	34
5	Simulation Parameters and Results	39
5.1	Mediterranean Maritime Environment	39
5.2	Simulation Parameters	43
5.3	Target Types and Material Properties	43
5.4	Results	45
5.5	Sensitivity Analysis	52
6	Conclusion	57
6.1	Summary of Findings	57
6.2	Future Research	58

Appendix A Auxiliary Functions for MATLAB Implementation	59
Appendix B Full MATLAB Propagation Code	63
List of References	71
Initial Distribution List	75

List of Figures

Figure 1.1	Typical power requirements for possible targets	5
Figure 2.1	Representation of the propagation of a Gaussian beam	9
Figure 2.2	Sunlight total extinction by the atmosphere as a function of wavelength (upper plot), and the constituents that make the major contribution to extinction (lower plot)	11
Figure 2.3	Illustration of optical turbulence causing light distortion and image blurring due to temperature variations in the atmosphere	12
Figure 2.4	Demonstration of the effect of turbulence on the intensity profile	13
Figure 2.5	The physics of thermal blooming effect on a laser beam	15
Figure 3.1	Schematic representation of Fresnel diffraction from a continuous source	20
Figure 3.2	The MATLAB functions for 2D Fourier transform and inverse Fourier transform	25
Figure 3.3	MATLAB function that creates the initial field	25
Figure 3.4	The code snippet that creates the initial field of a circular aperture	26
Figure 3.5	The code snippet that applies phase shift to the initial field	27
Figure 3.6	The concept of modeling atmospheric turbulence by using a series of 2D phase screens	28
Figure 3.7	Schematic representation of generating a realistic turbulent phase screen	28
Figure 4.1	Representation of a target area exposed to laser irradiation	32
Figure 4.2	Dimensionless melting time as a function of dimensionless absorbed power per unit length	36

Figure 4.3	Comparison of three melt-through times for the 3 mm thick aluminum target as a function of the power arrives at the target	37
Figure 4.4	Comparison of three melt-through times for the 10 mm thick stainless-steel target as a function of the power arrives at the target	38
Figure 5.1	The profile at 5 meters in the Mediterranean Sea, computed by NAVS-LaM using data from ERA5 for 12Z on September 1, 2017	40
Figure 5.2	Seasonal and daytime variations of the at 5 meters above the surface	41
Figure 5.3	Vertical turbulence profiles up to 3000 m across different seasons at four specific points in the Mediterranean region, based on median values at 09Z time	42
Figure 5.4	Predicted melt-through times for a patrol boat hull at four points in the Mediterranean Sea, showing variability across seasons for the 25th, 50th, and 75th percentile profiles	46
Figure 5.5	Predicted melt-through times for a radar antenna at four points in the Mediterranean Sea, showing variability across seasons for the 25th, 50th, and 75th percentile profiles	47
Figure 5.6	Predicted melt-through times for a cargo container at four points in the Mediterranean Sea, showing variability across seasons for the 25th, 50th, and 75th percentile profiles	48
Figure 5.7	Predicted melt-through times for a floating mine at four points in the Mediterranean Sea, showing variability across seasons for the 25th, 50th, and 75th percentile profiles	49
Figure 5.8	Predicted melt-through times for an amphibious vehicle at four points in the Mediterranean Sea, showing variability across seasons for the 25th, 50th, and 75th percentile profiles	50
Figure 5.9	Predicted melt-through times for aerial targets across four seasons at four specific points, based on the median values at 09Z time . . .	51
Figure 5.10	Sensitivity of melt-through time for a patrol boat hull to varying laser output power and range across different seasons at Point 1	53
Figure 5.11	Sensitivity of melt-through time to aluminum target thickness across four seasons at four specific points	54

THIS PAGE INTENTIONALLY LEFT BLANK

List of Tables

Table 2.1	Composition of the atmosphere	10
Table 3.1	Simulation parameters for validating FDM implementation	30
Table 3.2	Comparison of FDM and SLM results for model validation	30
Table 5.1	Parameters used in the simulation	43
Table 5.2	Target material properties and assumptions	44

THIS PAGE INTENTIONALLY LEFT BLANK

List of Acronyms and Abbreviations

COIL Chemical oxygen iodine laser

DF Deuterium fluoride

FDM Fresnel diffraction model

FEL Free-electron laser

HEL High energy laser

HF Hydrogen fluoride

NAVSLaM The navy atmospheric vertical surface layer model

SLM Scaling law model

SSL Solid-state laser

TOTEM The tropospheric optical turbulence ensemble of models

THIS PAGE INTENTIONALLY LEFT BLANK

Acknowledgements

I would like to express my appreciation to my advisor, Dr. Keith Cohn, and my co-advisor, Dr. Joseph Blau, for their guidance, assistance and motivation during this research project. Their expertise and insight were crucial in helping me complete this thesis.

I am also very thankful to Mr. Paul Frederickson for providing the atmospheric data that formed the foundation of my study.

I would like to extend my thanks to the Turkish Naval Forces for granting me the opportunity to pursue this master's program.

Lastly, I am deeply grateful to my wife, Hamide, for her support, understanding and love. Her dedication in caring for our newborn son, Esref, has provided me with the peace of mind and focus needed to complete this thesis.

THIS PAGE INTENTIONALLY LEFT BLANK

CHAPTER 1: Introduction

High energy lasers (HELs) are recognized as a game-changing technology with potential for enhancing maritime security and military capabilities. These laser weapons offer several advantages compared to traditional kinetic weapons [1]:

- Speed-of-light delivery: They enable rapid and precise engagement of targets.
- Precision engagement: They minimize collateral damage and provide improved accuracy.
- Scalability: They are adaptable to varying threat scenarios and engagement ranges.
- Reduced cost per shot: They offer a cost-effective alternative to expendable munitions.
- Large magazine: They have a virtually limitless magazine capacity constrained only by the available power supply.
- Absence of recoil: They enhance precision by eliminating the backward movement traditionally associated with firearms, ensuring stable and accurate engagements.

However, HELs face challenges associated with atmospheric effects, including absorption, scattering, and turbulence, which can significantly impact their range and effectiveness.

HELs are a promising technology providing a cost-effective, precise, and scalable solution for countering various targets in the maritime domain. However, the effectiveness of HELs in the Mediterranean maritime environment—a strategic region for the security and stability of Europe, Africa, and the Middle East—is not well-defined and requires further investigation. This is because the Mediterranean Sea has unique characteristics due to its semi-enclosed nature, which leads to higher salinity levels, more stable atmospheric conditions, and distinct humidity patterns [2]. These factors may affect the performance and reliability of the laser. This thesis aims to evaluate the effectiveness and limitations of HELs in the Mediterranean Sea under different atmospheric conditions.

1.1 Overview of High Energy Lasers

The concept of HELs is hardly new; it has undergone research and development since the 1970s. Presently, military forces globally, including the United States, Russia, China, United Kingdom, France, Pakistan, Germany, India, Iran and Turkiye are developing and testing HELs [3].

Some possible uses include targeting missiles, ground and air vehicles, and disabling or blinding sensors [4].

1.1.1 Types of High Energy Lasers

Over the years, there have been several main categories of laser technologies advanced for use in HEL weapons: chemical lasers, which utilize a chemical reaction to energize a gaseous medium; solid-state lasers (SSLs), which use optically stimulated gain media; and free-electron lasers (FELs), which use a relativistic electron beam as their lasing medium [5].

1.1.1.1 Chemical Lasers

Chemical lasers are powered by a chemical reaction and are distinct from other lasers that use electricity [6]. There are two main types of chemical lasers:

- Chemical Oxygen Iodine (COIL): It operates on an atomic electronic transition unlike other chemical lasers like hydrogen fluoride and deuterium fluoride that rely on molecular transitions [7]. It is known for its unique ability to generate high powers of multi-megawatts at a relatively short wavelength of 1315 nm, with singlet delta oxygen, which refers to a specific excited state of molecular oxygen, produced through a chemical reaction involving chlorine and basic hydrogen peroxide [6].
- Hydrogen Fluoride (HF) and Deuterium Fluoride (DF): HF/DF lasers produce a laser beam at 2.8 μm (HF) or 3.8 μm (DF) wavelengths [8]. They operate by chemically reacting fluorine with hydrogen or deuterium to create excited HF or DF molecules, which release energy as laser light.

The chemicals used are often hazardous, requiring careful handling and storage. Disposing of their waste products also poses a significant environmental contamination threat. The

operation of chemical lasers is complex, demanding precise control over both the chemical reaction and the laser environment, which can limit their operational scope [9].

1.1.1.2 Solid-State Lasers

In contrast to other lasers that may use gas, liquid, or plasma, SSLs utilize a solid substrate as the lasing medium. The phrase “solid-state” refers to the lasing material’s solid physical form [10]. These lasers have been pivotal in advancing laser technology. They are used in multiple fields, including manufacturing, material processing, medical and scientific studies. The core component of each SSL is the lasing medium, which is a solid such as ruby or neodymium-doped yttrium aluminum garnet (Nd:YAG). When this crystal absorbs photons from a pumping source like a flashlamp or another laser, its atoms are excited to a higher energy state. The atoms then typically decay through intermediate states before returning to their ground state, releasing photons. The presence of an optical cavity enables the amplification and oscillation necessary to generate coherent laser light [10].

There are several advantages of SSLs. (1) High output power: they are capable of delivering extremely high power, particularly when operating in continuous wave mode; (2) Electrically powered: They eliminate the need for complex chemical handling and provide a more reliable and easily scalable energy source; (3) Efficiency: These lasers are known for their high electrical-to-optical efficiency, especially when they are diode-pumped [11].

However, there are also challenges associated with SSLs: (1) Thermal management: the high power output can lead to substantial heat generation, necessitating effective thermal management to protect the laser components and ensure peak performance.; (2) Size scaling: The size of the laser system tends to scale up with the output power. This can be a limitation for applications requiring compact solutions [11].

1.1.1.3 Free-Electron Lasers

The theoretical foundation for FELs was established by H. Motz in 1951, with the first practical demonstration by R. Phillips in 1960 using the ubitron, and further development by J. Madey in 1971, who called the term “stimulated magnetic bremsstrahlung” [12].

FELs are devices that use a high energy electron beam’s interaction with a series of magnets arranged in a periodic structure, known as an undulator, to enhance electromagnetic

waves [12]. The core concept of FELs is based on stimulated emission, in which the interaction between an electron beam and an electromagnetic field produces coherent radiation.

A notable feature of FELs is their broad tunability [12]. The continuous adjustability of parameters allows for precise tuning of the emitted light's wavelength, and the broad range of longitudinal energy factors enables FELs to cover an extensive spectrum, from microwaves to X-rays [12]. However, they are large and emit ionizing radiation [13].

1.1.2 Applications in Maritime Environment

The maritime environment presents unique challenges and opportunities for the deployment of HELs. These weapons offer several advantages in a naval context. The ability to deliver power at the speed of light and with precision is highly valued. Here are some key applications of HELs in the maritime environment [4]:

- Ship defense against aerial threats: HELs can potentially intercept and neutralize incoming aerial threats, including missiles, drones, and aircraft.
- Coastal and port security: HEL systems enhance security by providing continuous surveillance and the ability to engage potential threats near coastlines and ports.
- Protection of high-value assets: Naval vessels, offshore platforms, and critical infrastructure can benefit from HELs for active defense. They safeguard valuable assets against attacks.
- Interference with adversary systems: HELs can disrupt or disable adversary sensors, communication systems, and optics. By interfering with their functionality, HELs degrade the adversary's capabilities.
- Boost-phase missile intercept: HELs can engage ballistic missiles during their boost phase (right after launch).

These varied applications of HELs highlight their profound ability to enhance naval capabilities [4].

Figure 1.1 shows typical laser power requirements for different kinds of targets. While soft targets, like sensors, can be neutralized with power levels as low as 100 W, a minimum power of 10 kW is needed for engaging hard targets [4].

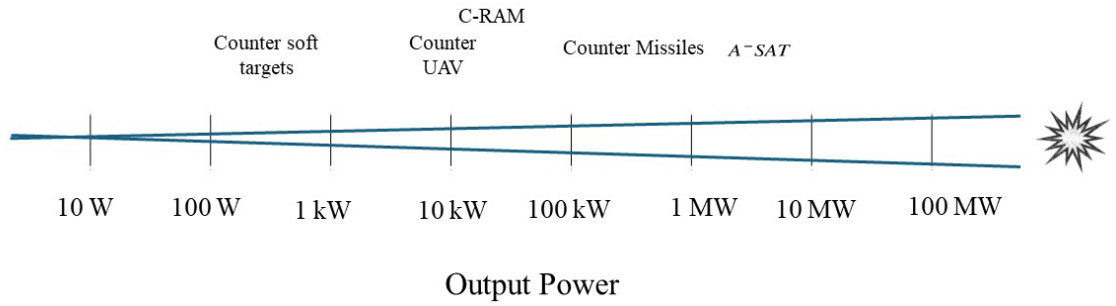


Figure 1.1. Typical power requirements for possible targets. Adapted from [4].

1.2 Thesis Structure and Overview

The second chapter of this thesis provides a concise introduction into the physical principles governing laser beam propagation. Chapter III introduces numerical methods employed in modeling the laser beam propagation. Chapter IV then explores the underlying physics responsible for the lethal mechanisms of HELs. The analysis culminates in Chapter V, where simulation parameters and results are presented and discussed. Finally, Chapter VI summarizes the key findings and offers concluding remarks.

THIS PAGE INTENTIONALLY LEFT BLANK

CHAPTER 2: Propagation Physics

This chapter delves into the fundamental principles governing laser light and its subsequent propagation through the Earth's atmosphere. We begin by exploring the properties of laser light; subsequently, we investigate how the laser energy, once emitted, propagates to a designated target.

2.1 Properties of Laser Light

This section establishes the fundamental properties of laser light relevant to its propagation characteristics. We begin by examining the three key properties that distinguish laser light from conventional sources: monochromaticity, directionality, and coherence. The discussion on directionality introduces the concept of the Gaussian beam profile, a crucial aspect for understanding beam behavior. Finally, the concept of beam quality factor (M^2) is introduced, a parameter that encompasses the overall quality of a laser beam for propagation purposes.

2.1.1 Coherence

In everyday life, the light we usually observe, such as sunlight or the glow from a bulb, is incoherent: emitting light with a broad range of wavelengths and random phases. On the other hand, lasers emit beams of coherent light with waves that are in phase with each other over a narrow range of wavelengths [14]. This unique property allows a laser beam to be focused to a small spot unlike the light from incoherent sources. The coherence of laser light makes it ideal for a variety of uses, including the development of directed energy weapons.

The coherence of laser light is crucial and refers to how different parts of the light wave are correlated with each other. There are two types of coherence: temporal and spatial coherence [14].

Temporal coherence measures how well a wave maintains a phase relationship over time. A laser beam with high temporal coherence will have a precise frequency and wavelength

resulting in a narrow bandwidth in its spectrum, which helps minimize atmospheric attenuation [14].

On the other hand, spatial coherence looks at how different points in space within a laser beam correlate with each other. It describes how the wavefront evolves spatially. Laser beams with high spatial coherence display well-defined beam profiles and can create sharp interference patterns [14].

The beam quality factor, M^2 plays a role in assessing the laser beam's quality. It is literally a measure of spatial coherence. It indicates how well a laser beam can be focused, which is vital for numerous practical uses [15].

The quality factor M^2 , which is dimensionless and never less than 1, is used to explain how much a laser beam diverges from the Gaussian beam. A perfect Gaussian beam with an M^2 value of 1 shows diffraction-limited performance. If the M^2 value is higher, it means the beam deviates more from the Gaussian profile, indicating reduced beam quality [15].

2.1.2 Transverse and Longitudinal Behavior

Transverse behavior of laser light refers to how it evolves perpendicular to the direction of propagation. A laser beam's shape and uniformity are determined by transverse behavior. Longitudinal behavior, however, refers to changes along the path of propagation, defining coherence length and the spatial extent of a laser pulse in the propagation direction. The transverse mode profile shows how the intensity of the beam varies across the beam's diameter. For example, a Gaussian mode produces what we know as the characteristic bell-shaped distribution. The beam profile, the divergence angle, the beam waist and the Rayleigh range are the most important features that govern how a laser beam behaves [15]:

- Gaussian beam profile means the intensity distribution across a beam diameter is distributed in a Gaussian manner.
- Divergence angle (θ) is defined as the angle at which beam spreads away from the waist. It depends on the initial diameter of the laser beam and the wavelength of the laser. This determines whether it is focusable over a certain range and how focusable it is.

- Beam waist (w_0) is the radius of the beam at its minimum value. The beam waist is of key importance for both focusing the beam and determining its intensity.
- Rayleigh Range (Z_r) is the range over which a laser beam remains nearly collimated. It is defined by

$$Z_r = \frac{\pi w_0^2}{\lambda}, \quad (2.1)$$

where λ is the wavelength. It is the distance at which the cross-sectional area of the beam has grown to twice its value at the waist. A shorter Rayleigh range means that the beam will diverge more quickly, and a longer Rayleigh range indicates that the beam can remain collimated over a longer distance [15].

Figure 2.1 shows how a Gaussian beam evolves as it propagates, starting from a narrow waist, expanding to the Rayleigh range, and eventually becoming wider. However, it still maintains a Gaussian-shaped beam in the far-field.

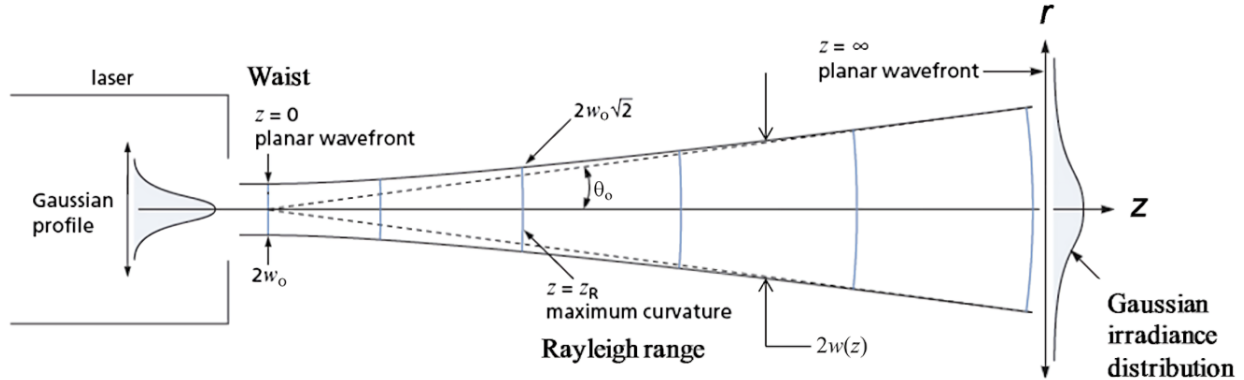


Figure 2.1. Schematic representation of the propagation of a Gaussian beam.
Source: [15].

2.2 Atmospheric Effects on Laser Propagation

The atmosphere is made of molecular gases and aerosols in the form of suspended particulates. In Table 2.1, a composition of atmosphere is listed in descending order of abundance. The fractions demonstrate the average values; they may vary depending on location, altitude, and time of day.

Table 2.1. Composition of the atmosphere. Adapted from [16].

Constituent	Fraction	Constituent	Fraction
Nitrogen (N_2)	78.08 %	Methane (CH_4)	2 ppm
Oxygen (O_2)	20.95 %	Krypton (Kr)	1 ppm
Argon (Ar)	0.93 %	Hydrogen (H_2)	0.5 ppm
Water (H_2O)	0-4 %	Nitrous oxide (N_2O)	0.3 ppm
Carbon dioxide (CO_2)	325 ppm	Carbon monoxide (CO_3)	0.05-0.2 ppm
Neon (Ne)	18 ppm	Ozone (O)	0.02 - 10 ppm
Helium (He)	5 ppm	Xenon (Xe)	0.08 ppm

HEL beam propagation in the atmosphere is a complicated physical phenomenon, which is influenced by four main factors: absorption, scattering, turbulence-induced beam spreading, and thermal blooming [17].

2.2.1 Extinction

When a laser beam comes into contact with molecules and aerosols in the atmosphere, it may be absorbed or scattered [18]. The reduction in radiation, by any process in which photons are converted into heat or excitation energy as a beam passes through a given medium, is called absorption. The process, by which radiation is reduced by redirecting some of the photons, is called scattering [19]. Extinction is the total effect of both absorption and scattering on a laser beam, and its effect can be estimated by the Beer-Lambert Law:

$$P(R) = P_0 e^{-\int_0^R \varepsilon(z) dz}, \quad (2.2)$$

where P_0 is the output power at the beam director, $P(R)$ is the power after the beam travels a distance R , and $\varepsilon(z)$ is the extinction coefficient as a function of the beam path that accounts for the total loss due to both absorption and scattering. The upper plot in Figure 2.2 shows the extinction of sunlight (total absorption and scattering, as a percentage) going through the atmosphere as a function of wavelength, from 0.2 μm (ultraviolet) to 70 μm (far infrared). The lower plots show the main contributors of extinction. We can see that the extinction of

infrared light, in particular, is dominated by water vapor and carbon dioxide. At the shorter wavelengths, extinction is almost entirely due to absorption by oxygen and ozone, and also by Rayleigh scattering. We can infer from these plots that there are several wavelength windows where the atmosphere is extremely transparent to sunlight. A laser beam operating at one of these wavelengths is going to experience relatively little extinction. Shorter wavelengths also tend to suffer less diffraction, thus approximately 1 μm wavelength is ideal for HEL beam propagation [14].

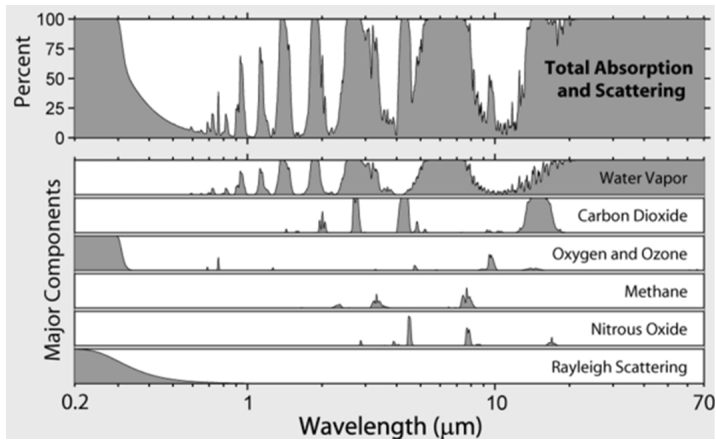


Figure 2.2. Sunlight total extinction by the atmosphere as a function of wavelength (upper plot), and the constituents that make the major contribution to extinction (lower plot). Source: [20].

2.2.2 Optical Turbulence

Optical turbulence refers to random fluctuations in the refractive index of air due to random changes in the wind velocity, temperature, and density. This causes (1) beam wander, which results in pointing errors and reduced accuracy; and (2) beam spreading, which leads to a reduction of the intensity of the laser beam with increasing distance [17].

Light rays that pass through regions of different refractive indices are bent according to Snell's law. Although the refractive index of air is nominally close to 1, small fluctuations from this value due to turbulence can cause the beam to spread or break apart over a long propagation path [18]. Figure 2.3 shows how light rays get bent and distorted when they pass through regions of air with different temperatures, known as turbulent cells. These

cells cause the light rays to change their direction slightly, leading to a blurred appearance of distant objects, like the image shown in the right [14].

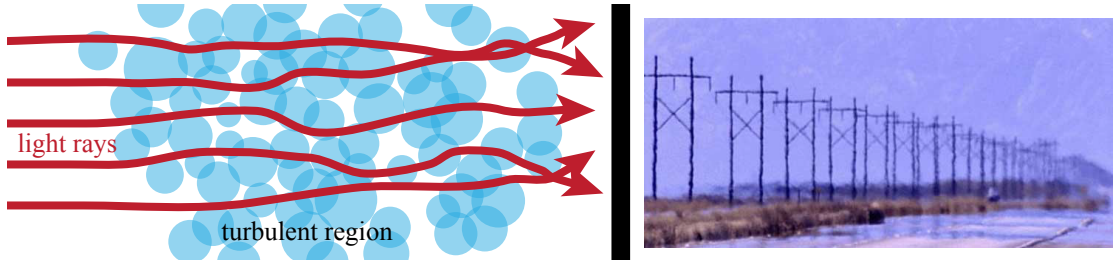


Figure 2.3. Illustration of optical turbulence causing light distortion and image blurring due to temperature variations in the atmosphere. Source: [14].

The refractive structure constant, also referred to by the symbol C_n^2 , is a mathematical quantity representing the strength of atmospheric turbulence. It is defined by

$$C_n^2(\mathbf{r}) = \frac{\langle [n(\mathbf{r}) - n(\mathbf{r} + \Delta\mathbf{r})]^2 \rangle}{|\Delta\mathbf{r}|^{2/3}}, \quad (2.3)$$

where \mathbf{r} is the position of interest, n is the refraction index, and $\langle \dots \rangle$ indicates the average over a sphere of radius Δr centered on that point. Typical values of C_n^2 vary between $10^{-17} \text{ m}^{-2/3}$, which corresponds to very mild turbulence effects, and $10^{-12} \text{ m}^{-2/3}$ which indicates strong turbulence effects [17]. Figure 2.4 illustrates the impact of turbulence on the irradiance profile at the target plane over an engagement distance of 3 km. The leftmost plot represents very mild turbulence, which results in negligible distortion of the laser beam. The middle plot shows the effect of moderate turbulence, which visibly distorts the beam. The rightmost plot demonstrates severe turbulence, leading to significant distortion and a visible reduction in the irradiance.

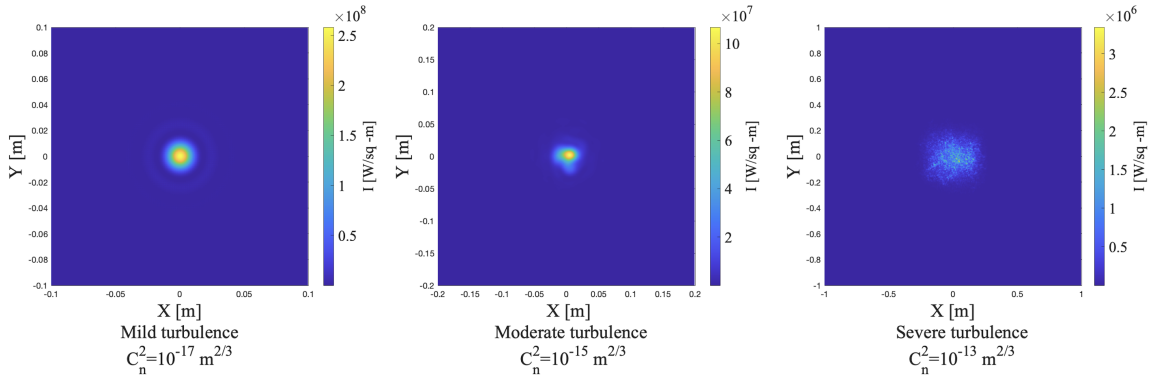


Figure 2.4. Demonstration of the effect of turbulence on the intensity profile at the target plane over a 3 km engagement distance with three different C_n^2 values.

The refractive index structure constant C_n^2 represents the local turbulence strength, and the integrated effect of the turbulence encountered along a beam's path can be estimated by integrating the C_n^2 values, weighted according to distance, over the total path—resulting in a value called the Fried parameter (r_0) [21]. It is a length defined as

$$r_0 = \left[0.423k^2 \int_0^R C_n^2(z) \left(1 - \frac{z}{R}\right)^{5/3} dz \right]^{-3/5}, \quad (2.4)$$

where 0.423 is a dimensionless fitting parameter, k is the wavenumber and R is the target range. Smaller values of r_0 imply stronger turbulence. If the beam director diameter is less than the Fried parameter, the effect of the turbulence could be disregarded. However, for typical HEL parameters, the director diameter is often greater than the Fried parameter. Thus, the effects of turbulence should be taken into account in HEL applications [14].

To illustrate this, consider the following example with typical parameters:

- $R = 3 \text{ km}$
- $C_n^2 = 10^{-14} \text{ m}^{-2/3}$ (constant along the path)
- $\lambda = 1 \mu\text{m}$
- $k = 2\pi/\lambda = 6.28 \cdot 10^6 \text{ m}^{-1}$

The Fried parameter is calculated to be 4.3 cm, which is less than beam director diameters that are generally used in HEL applications, where values are generally greater than 10 cm.

2.2.3 Thermal Blooming

Thermal blooming is a type of laser beam distortion that can occur when the energy in a high-power laser beam is absorbed in the air or other medium through which it propagates. As a result of this absorption, the air or other medium along the optical path locally heats up, and its refractive index changes due to the thermal expansion. These changes in the refractive index of the medium where the light is propagating create local variations in the optical length, which deform the laser beam [22].

The thermal blooming effect is depicted in Figure 2.5. Figure 2.5 (a) depicts the irradiance profile of a standard laser beam, and Figure 2.5 (b) illustrates the correlated temperature profile, which simply mirrors the intensity profile due to the linear relationship between the absorption energy and intensity. As temperature increases, the density decreases as illustrated in Figure 2.5 (c), and the refractive index also decreases as shown in Figure 2.5 (d), since the air refraction index is directly proportional to the density. The result is that the heated air acts as a defocusing lens, causing the beam to spread, thus decreasing the irradiance on a target [18].

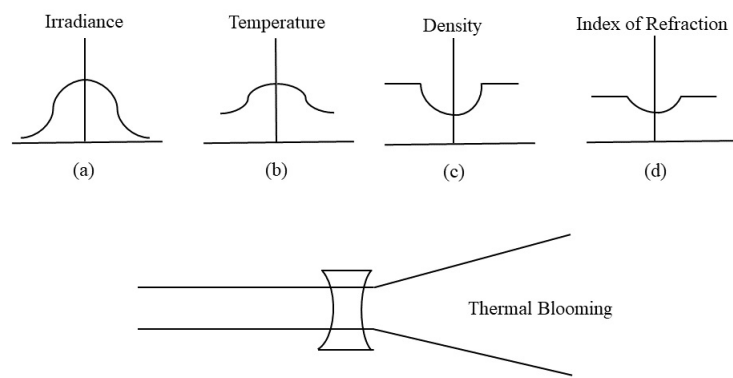


Figure 2.5. The physics of thermal blooming effect on a laser beam. Adapted from [18].

THIS PAGE INTENTIONALLY LEFT BLANK

CHAPTER 3: Numerical Models

Predicting the irradiance of a laser beam at the target after propagating through the atmosphere is not an easy task. There is no precise analytical solution to estimate the irradiance at the target. Thus, models are needed for predicting the irradiance. Among the various models currently in use, a Scaling Law Model (SLM) and a Fresnel Diffraction Model (FDM) were selected to simulate the laser beam propagation in this thesis. The SLM was chosen for its rapid and reasonably accurate predictions, while the FDM was selected for its higher accuracy.

3.1 Scaling Law Model

This model is based on the scaling law codes developed by the Directed Energy Group in the NPS Physics Department. It provides a rapid prediction of the time-averaged irradiance at the target with an accuracy within 20% of the experimental results [14].

3.1.1 The Time-averaged Spot Radius

For the calculations, the laser beam is assumed to uniformly fill the beam director, with a constant amplitude and phase across the mirror, and the beam director is assumed to have a focal length of f_l so as to focus the laser beam onto the target at the distance R . There are three main effects that add up to the overall spot radius [14]:

- The effect of diffraction can be estimated by

$$w_d \approx (0.594) \lambda \frac{R}{D}, \quad (3.1)$$

where 0.594 is a dimensionless fitting parameter, w_d is the diffraction contribution to the spot radius, λ is the wavelength, R is the range, and D is the beam director diameter.

- The effect of turbulence can be approximated by

$$w_t \approx \frac{2\lambda R}{\pi r_0}, \quad (3.2)$$

where w_t is the turbulence contribution to the spot radius and r_0 is the Fried parameter, which is determined using Equation 2.4.

- The effect of jitter may be caused by platform motion and tracking error and can be estimated by

$$w_j \approx \theta_{rms} R, \quad (3.3)$$

where w_j is the jitter contribution to the spot radius, and θ_{rms} is the average angular variance in radians.

The overall time-averaged spot radius can be estimated from all of these three effects by adding the contributions in quadrature to obtain

$$\langle w_{tot} \rangle \approx \sqrt{w_d^2 + w_t^2 + w_j^2}. \quad (3.4)$$

3.1.2 The Time-averaged Irradiance

The time-averaged irradiance at the target can be approximated using Equation 2.2 which calculates the power at the target divided by the spot size area. The equation is given by

$$\langle I_t \rangle \approx \frac{P_0}{\pi \langle w_{tot} \rangle^2} \exp \left(- \int_0^R \varepsilon(z) dz \right), \quad (3.5)$$

where P_o is the output power of the laser, and ε is the atmospheric extinction coefficient [14].

To illustrate the calculation of time-averaged irradiance, consider the following example with the parameters given below:

- $\lambda = 1 \mu\text{m}$
- $R = 3 \text{ km}$
- $D = 20 \text{ cm}$

- $\theta_{rms} = 0$ (neglecting jitter effect)
- $C_n^2 = 10^{-14} \text{ m}^{-2/3}$ (constant along the path)
- $\varepsilon = 10^{-4} - 10^{-5} \text{ m}^{-1}$ (linearly decreasing from 10^{-4} m^{-1} to 10^{-5} m^{-1})
- $P_0 = 20 \text{ kW}$.

Given these parameters, the diffraction contribution w_d is calculated to be 8.9 mm. For a constant C_n^2 profile of 10^{-14} along the 3 km path, the Fried parameter, r_0 , is calculated to be 4.5 cm. Consequently, the turbulence contribution w_t is found to be 4.4 cm. Given these values, the overall time-averaged spot radius, $\langle w_{tot} \rangle$, is approximately 4.5 cm. Thus, the time-averaged irradiance at the target is approximately 0.26 kW/cm^2 .

In subsequent calculations for this thesis, the jitter effect is assumed to be negligible.

3.2 Fresnel Diffraction Model

For the scenarios where the turbulence changes significantly along the path to the target, more accurate models than the SLM are required. The FDM provides more precise results compared to the previously discussed model. However, it demands significantly higher computational time and is therefore much slower. To give a comparison, SLM produces results in under 10 seconds regardless of atmospheric conditions, while FDM calculations are on the order of hours even for moderate conditions. The computation time for FDM is directly proportional to the number of phase screens (determined according to the turbulence strength), the number of realizations, and the number of grid points. The FDM involves numerically solving approximations to Maxwell's wave equation, accounting for diffraction and atmospheric effects at each step [14].

3.2.1 Diffractions from Continuous Sources

A schematic representation of Fresnel diffraction is illustrated in Figure 3.1. The source, whose plane is defined by a coordinate system (x_s, y_s) , emits waves that propagate a distance r to the point P on the target screen, whose plane is defined by a coordinate system (x, y) .

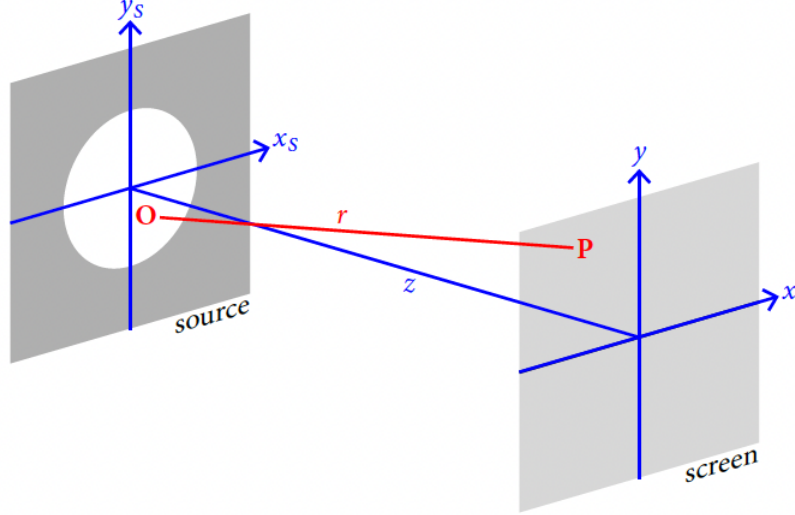


Figure 3.1. Schematic representation of Fresnel diffraction from a continuous source. Source: [14].

In this case, the complex electric field ($\tilde{E}_{tot}(x, y)$) at the point P can be estimated by

$$\tilde{E}_{tot}(x, y) = \frac{1}{i\lambda} \iint \frac{\tilde{E}_0(x_s, y_s)}{r} e^{i(\mathbf{k} \cdot \mathbf{r} - \omega t)} dx_s dy_s, \quad (3.6)$$

where $\tilde{E}_0(x_s, y_s)$ is the electric field at point O on the source, \mathbf{k} is the wave vector with a magnitude of $2\pi/\lambda$, ω is the angular frequency, t is the time, and \mathbf{r} is the position vector, whose magnitude is given by

$$r = \sqrt{(x_s - x)^2 + (y_s - y)^2 + z^2}. \quad (3.7)$$

Equation 3.6 is very hard to calculate, even numerically. However, reasonable approximations can be applied to simplify the process.

3.2.2 The Paraxial Approximation

In a typical HEL engagement scenario, the target is generally located at a significant distance from the source, leading to the dominance of the z-component in Equation 3.7. As such, the

distance r can be approximated as z under the zeroth-order approximation, resulting in the simplification of Equation 3.6 as follows:

$$\tilde{E}_{tot}(x, y) = \frac{1}{i\lambda z} \iint \tilde{E}_0(x_s, y_s) e^{i(\mathbf{k} \cdot \mathbf{r} - \omega t)} dx_s dy_s. \quad (3.8)$$

We cannot simply replace r in the exponential term with z , as it is more sensitive to small changes and such an approximation may lead to errors. However, we can factor out z in Equation 3.7 and obtain

$$r = z \sqrt{1 + \frac{(x_s - x)^2}{z^2} + \frac{(y_s - y)^2}{z^2}}. \quad (3.9)$$

Given that z is significantly larger than the terms in the numerators of Equation 3.9, we can apply a Taylor expansion of r . Retaining only the first-order terms in the expansion, we obtain

$$r = z + \frac{x^2 + y^2}{2z} + \frac{x_s^2 + y_s^2}{2z} - \frac{x_s x + y_s y}{z}. \quad (3.10)$$

If we substitute r in Equation 3.6 with Equation 3.10, and factor out all terms that do not depend on the integration variable, we obtain

$$\tilde{E}_{tot}(x, y) = \tilde{C} \iint \tilde{E}_0(x_s, y_s) e^{i\frac{\mathbf{k}}{2z}(x_s^2 + y_s^2)} e^{-i\frac{\mathbf{k}}{z}(x_s x + y_s y)} dx_s dy_s, \quad (3.11)$$

where \tilde{C} is

$$\tilde{C} = \frac{1}{i\lambda z} e^{i(kz - \omega t)} e^{i\frac{\mathbf{k}}{2z}(x^2 + y^2)}. \quad (3.12)$$

In deriving Equation 3.11, we implicitly assume that the wave vector \mathbf{k} is aligned along the z-axis. This simplifies the exponential term to depend primarily on the z-component of the propagation.

3.2.3 Fresnel Diffraction with Fourier Transforms

A two-dimensional Fourier transform is given by

$$\tilde{G}(f_x, f_y) = \iint_{-\infty}^{\infty} \tilde{g}(x, y) e^{-2\pi i(f_x x + f_y y)} dx dy \equiv \mathcal{F}(\tilde{g}(x, y)), \quad (3.13)$$

where \mathcal{F} is the Fourier transform operator.

Equation 3.11 is very similar to a 2D Fourier transform and can be easily expressed in terms of a Fourier transform by applying the following substitutions:

$$(x, y) \rightarrow (x_s, y_s), \quad (3.14)$$

$$\tilde{g}(x, y) \rightarrow \tilde{E}_0(x_s, y_s) e^{i \frac{k}{2z} (x_s^2 + y_s^2)}, \quad (3.15)$$

$$f_x \rightarrow \frac{x}{\lambda z}, \quad (3.16)$$

$$f_y \rightarrow \frac{y}{\lambda z}, \quad (3.17)$$

$$dxdy \rightarrow dx_s dy_s. \quad (3.18)$$

Consequently, the Fresnel diffraction integral can be written as

$$\tilde{E}_{tot}\left(\frac{x}{\lambda z}, \frac{y}{\lambda z}\right) = \tilde{C} \left\{ \mathcal{F} \left[\tilde{E}_0(x_s, y_s) e^{i \frac{k}{2z} (x_s^2 + y_s^2)} \right] \right\}. \quad (3.19)$$

However, this approach has a downside: we have no control over the magnification parameter, M , which is given as the ratio of the target plane size to the source plane size. The target plane size is determined by the source plane with the following relation:

$$\Delta x = \frac{\lambda z}{N \Delta x_s} \text{ and } \Delta y = \frac{\lambda z}{N \Delta y_s}, \quad (3.20)$$

where Δx and Δy are the target plane grid spacing, Δx_s and Δy_s are the source plane grid spacing, and N is the number of grid points in each direction. This unwanted dependency may pose resolution problems, as the target grid spacing may not be small enough to capture significant details. While the target grid spacing can be made sufficiently small by increasing the number of grid points, this comes at the cost of increased computational burden [14].

3.2.4 Fresnel Diffraction with Convolution Theorem

In order to control the magnification parameter, the convolution theorem can be applied to the Fresnel diffraction integral. The convolution operation is given by

$$f(x, y) \otimes g(x, y) = \iint f(x', y') g(x - x', y - y') dx' dy'. \quad (3.21)$$

This can also be represented as the inverse Fourier transform of the product of the Fourier transforms of the functions, given by

$$f(x, y) \otimes g(x, y) = \mathcal{F}^{-1} \{ \mathcal{F}[f(x, y)] \mathcal{F}[g(x, y)] \}. \quad (3.22)$$

If we rewrite Equation 3.11 in the following form:

$$\tilde{E}_{tot}(x, y) = \frac{1}{i\lambda z} e^{i(kz - \omega t)} \iint \tilde{E}_0(x_s, y_s) e^{i\frac{k}{2z}[(x-x_s)^2 + (y-y_s)^2]} dx_s dy_s, \quad (3.23)$$

we can easily see the similarity with Equation 3.21. By making the substitutions given below:

$$f(x, y) \rightarrow \tilde{E}_0(x, y), \quad (3.24)$$

$$g(x, y) \rightarrow \frac{1}{i\lambda z} e^{i(kz - \omega t)} e^{i\frac{k}{2z}(x^2 + y^2)}, \quad (3.25)$$

$$x' \rightarrow x_s, \quad (3.26)$$

$$y' \rightarrow y_s, \quad (3.27)$$

Equation 3.23 can be expressed as a convolution by

$$\tilde{E}_{tot}(x, y) = \left\{ [\tilde{E}_0(x, y)] \otimes \left[\frac{1}{i\lambda z} e^{i(kz - \omega t)} e^{i\frac{k}{2z}(x^2 + y^2)} \right] \right\}. \quad (3.28)$$

By representing the Fresnel diffraction as a convolution, we get the ability to adjust the size of the target plane independently of the source plane.

3.2.5 MATLAB Implementation

Before introducing the MATLAB implementation of the Fresnel Diffraction convolution, it is necessary to define some auxiliary functions. Figure 3.2 illustrates the MATLAB function for 2D Fourier transform and inverse Fourier transform. The built-in MATLAB functions “fft2” and “ifft2” cannot be used directly because it requires a specific ordering of the argument matrix. This issue is resolved by using the built-in “fftshift” and “ifftshift” functions, which adjust the matrix order for us.

The MATLAB function that creates the initial field for a uniformly illuminated circular aperture on a source grid is presented in Figure 3.3. It gives the grid coordinates and the field amplitude in the circular aperture.

```

1 function [G] = ft2D(g,dxs)
2 % g = original source (2D complex matrix)
3 % G = Fourier transform of g
4 % dxs = grid spacing of g
5 G = fftshift(fft2(fftshift(g)))*dxs^2;
6 end
7 function g = ift2D(G,df)
8 % g = original source (2D complex matrix)
9 % G = Fourier transform of g
10 % df = discrete frequency spacing
11 N = size(G,1);
12 g = ifftshift(ifft2(ifftshift(G))) * (N*df)^2;
13 end

```

Figure 3.2. The MATLAB functions for 2D Fourier transform and inverse Fourier transform. Source: [14].

```

1 function [Xs,Ys,E] = circ(Ws,R,N)
2 % Ws = width of source grid [m]
3 % R = radius of circular aperture [m]
4 % N = number of grid points along each dimension
5 % Xs,Ys = coordinates of source grid (2D array)
6 % E = source field (2D array) [unit amplitude]
7 dxs = Ws/N; % source grid spacing
8 % source grid coordinates
9 [Xs, Ys] = meshgrid(-0.5*Ws + (0:N-1)*dxs);
10 r = sqrt(Xs.^2 + Ys.^2); % radial distance from origin
11 % create uniform field inside aperture
12 E = double(r<R); % amplitude 1 for r<R
13 %E(r==R) = 0.5; % amplitude 0.5 for r=R
14 end

```

Figure 3.3. MATLAB function that creates the initial field for a circular aperture. Source: [14].

The MATLAB function “fresnel_conv” [14], which calculates the Fresnel diffraction of a complex field E_0 from the source plane to the target plane using the convolution theorem, is presented in Appendix A. This method involves a series of Fourier transforms and phase factor multiplications.

3.2.5.1 Creating Initial Field at the Source

The irradiance at the source can be calculated by

$$I_0 = \frac{P_0}{\pi a^2}, \quad (3.29)$$

where P_0 is the output power of the HEL, and a is the beam director radius. Therefore, the initial electric field amplitude at the source can be estimated by

$$E_0 = \sqrt{\frac{2I_0}{c\varepsilon_0}}, \quad (3.30)$$

where c is the speed of light, and ε_0 is the vacuum permittivity constant. This calculation can be implemented in MATLAB using the code snippet presented in Figure 3.4.

```

1 % initial field at beam director
2 E0 = sqrt (2* P0 / (c* eps0 *pi*a^2));
3 Xs ,Ys ,Es ]= circ (Ws,a ,N);
4 Es=E0*Es;
```

Figure 3.4. The code snippet that creates the initial field of a circular aperture.

Source: [14].

3.2.5.2 Applying Phase Shift to the Initial Field

The initial flat field with a constant phase becomes curved and focused when it passes through the curved mirror in the beam director. The thickness difference across the mirror (thicker in the middle) causes a phase shift because photons travel more slowly in glass than air and experience delays in thicker parts of the mirror. The phase shift caused by a curved mirror with a focal length of f_l is given by

$$\phi(x_s, y_s) = -\frac{k}{2f_l} \left(x_s^2 + y_s^2 \right), \quad (3.31)$$

where $k = 2\pi/\lambda$. The phase shift is zero at the center of the lens and increases outward. To apply this phase shift, the field is multiplied by $e^{i\phi(x_s, y_s)}$. This phase shift can be implemented in MATLAB using the code snippet presented in Figure 3.5.

```

1 % focus onto target
2 f1 = 5000; % focal length [m]
3 k = 2*pi/lambda; % wavenumber [1/m]
4 phi = -k/(2*f1)*(Xs.^2 + Ys.^2); % phase shift
5 Es = Es.*exp(1i*phi); % apply to wavefront

```

Figure 3.5. The code snippet that applies phase shift to the initial field.
Source: [14].

3.3 Modeling of a Turbulent Atmosphere

The instantaneous effect of the turbulence on the laser beam will be discussed in this section.

3.3.1 Phase Screen Approach

Turbulence is a three-dimensional effect, but the numerical diffraction technique considers two-dimensional grids. To overcome this mismatch, the propagation between the source and target can be divided into multiple steps, each with a randomized phase screen that represents the turbulence for that propagation step [14]. Each phase screen mimics wavy glass plates, representing the phase shift caused by the local turbulence. Figure 3.6 illustrates the concept of modeling atmospheric turbulence by using a series of two-dimensional phase screens. These phase screens are positioned at intervals, Δz , along the propagation path from the source plane to the target plane.

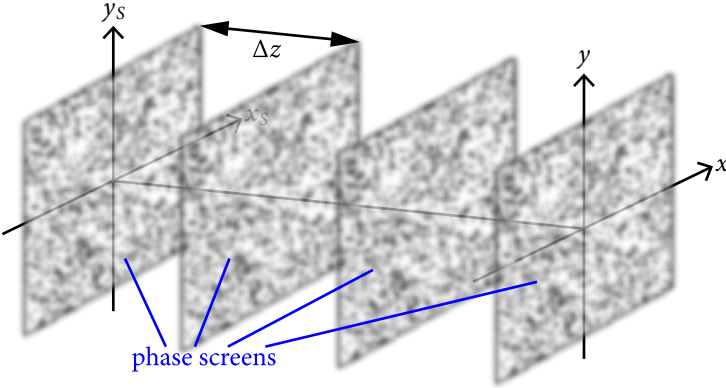


Figure 3.6. The concept of modeling atmospheric turbulence by using a series of 2D phase screens. Source: [14].

3.3.2 Kolmogorov Spectrum of Turbulence

In simpler terms, the phase screens are generated by summing many spatially varying sine functions with random wavelengths and directions, similar to summing a 2D Fourier series [14]. Figure 3.7 illustrates this process by adding many simple sinusoidal phase screens with random properties.

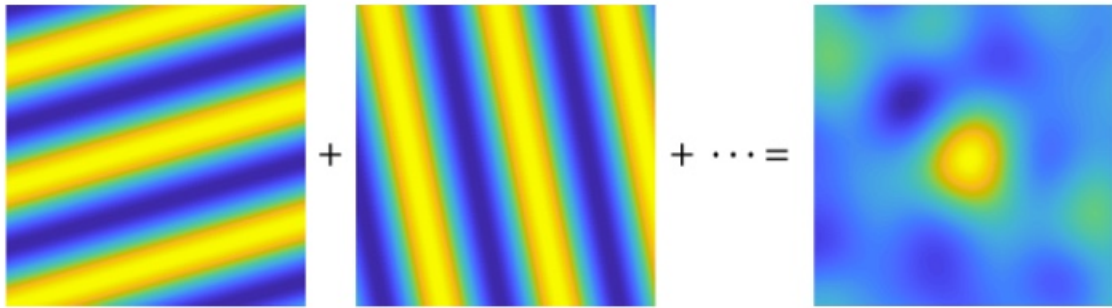


Figure 3.7. Schematic representation of generating a realistic turbulent phase screen. Adapted from [14].

More formally, the turbulence phase screen can be represented as a weighted sum of sinusoidal components [14]:

$$\phi_{ps}(x, y) = \sum_{n=-\infty}^{\infty} \sum_{m=-\infty}^{\infty} \tilde{c}_{n,m} e^{[2\pi i(f_{x,n}x + f_{y,m}y)]}, \quad (3.32)$$

where $f_{x,n}$ and $f_{y,m}$ are discrete spatial frequencies in the x and y directions, respectively, and $\tilde{c}_{n,m}$ are complex weighting coefficients. The selection of these coefficients is crucial for modeling a realistic atmosphere.

In the 1940s, Russian mathematician Andrey Kolmogorov proposed the widely accepted statistical model of choosing the reliable $\tilde{c}_{n,m}$ coefficients. According to his model, these coefficients can be determined by the following equation:

$$\left\langle \left| \tilde{c}_{n,m} (f_{x,n}, f_{y,m}) \right|^2 \right\rangle = \frac{\Phi(f_x, f_y)}{W^2}, \quad (3.33)$$

where W is the transverse width of the phase screen, and $\Phi(f_x, f_y)$ is the power spectrum of the turbulence. The power spectrum is related to the amount of each spatial frequency component in the phase screen. The Kolmogorov power spectrum can be calculated by

$$\Phi(f) = (0.023) r_{0,pw}^{-5/3} f^{-11/3}, \quad (3.34)$$

where $f = \sqrt{f_x^2 + f_y^2}$, and $r_{0,pw}$ is the Fried parameter of the plane wave, which can be calculated by

$$r_{0,pw} = \left(0.423 k^2 C_n^2 \Delta z \right)^{-3/5}. \quad (3.35)$$

MATLAB functions that generate a phase screen are presented in Appendix A. The functions are adapted from [14], [23].

3.4 Model Validation

To validate the proper implementation of the FDM, an example simulation of propagation through a constant turbulent atmosphere was conducted with the parameters presented in Table 3.1.

Table 3.1. Simulation parameters for validating FDM implementation.

Parameter	Value
Number of grid points (N)	512
Output power (P_0)	100 kW
Beam director radius (a)	2.5 cm, 10 cm, 25 cm
Window width in source plane (W_s)	20^*a
Window width in target plane (W)	90 cm, 45 cm, 35 cm
Wavelength (λ)	1 μ m
Extinction coefficient (ε)	10^{-4} m $^{-1}$
Refractive structure constant (C_n^2)	10^{-15} m $^{-2/3}$
Range (R)	3000 m
Number of turbulent phase screens	30
Number of realizations	100

The simulation was performed using three different beam director radii for both the SLM and the FDM. To obtain the peak irradiance, the irradiance distribution at the target plane was fit with a Gaussian curve in both the x and y directions. The spot radius was estimated as the standard deviation of the Gaussian fit. This process was averaged over 100 realizations to ensure accuracy. The results are presented in Table 3.2. For a constant turbulent atmosphere, the SLM can be considered as the theoretical solution. As evident from the results, our FDM agrees well with the SLM with a maximum difference of 15%. The full MATLAB propagation code for model validation is presented in Appendix B. The MATLAB code is adapted from [14].

Table 3.2. Comparison of FDM and SLM results for model validation.

Director Radius	SLM		FDM	
	Spot Radius (w)	Irradiance (I_{peak})	Spot radius (w)	Irradiance (I_{peak})
2.5 cm	3.73 cm	1.69 kW/cm 2	3.78 cm	1.44 kW/cm 2
10 cm	1.42 cm	11.63 kW/cm 2	1.31 cm	10.99 kW/cm 2
25 cm	1.17 cm	17.34 kW/cm 2	1.11 cm	15.53 kW/cm 2

CHAPTER 4: Lethality Physics

The lethality of HEL systems is their capacity to focus energy on a target, resulting in thermal and structural damage within seconds. The damage mechanism of HELs can be classified into three main categories [24]:

- Melting: The process of melting involves heating the material to its melting point and then adding energy to transform it from a solid to a liquid state. The geometrical (size, thickness) and thermal (specific heat, diffusivity, melting temperature, heat of fusion, etc.) properties of the target, the spot size and irradiance of the laser beam all play a role in the time it takes to melt through a target.
- Ablation: Ablation is the transformation of the material from solid to gas and requires significantly more power than melting.
- Burning: This mechanism is heating the material to its ignition temperature, which is generally higher than the melting temperature, and initiating a chemical reaction with oxygen that causes the material to ignite and burn [24].

This thesis focuses on melting as the primary damage mechanism, and performance analysis is conducted based on melt-through times.

4.1 Laser Interaction with Materials

When a laser beam interacts with materials, some portion of the beam power is reflected and the rest is absorbed. Absorbed power deposits energy into the material and, as a result, the temperature of the material rises. In order to better understand this interaction, we need to define some important terms:

- Irradiance (I): This is the power per unit area on the target's surface and a measure of how well the power is concentrated. It is usually measured in watts per meter squared (W/m^2) and can be estimated by

$$I = \frac{P_0 e^{-\int_0^R \varepsilon(z) dz}}{A}, \quad (4.1)$$

where P_0 is the output power at the beam director, $\varepsilon(z)$ is the atmospheric extinction coefficient of the beam path that accounts for the total loss due to both absorption and scattering effects, R is the distance of the target, and A is the illuminated area at the target's surface.

- Absorbed power (P_{abs}): This is the rate of energy delivery to the target after accounting for the atmospheric losses and reflected power. It is usually measured in watts (W) and can be estimated by

$$P_{abs} = \alpha I A, \quad (4.2)$$

where α is the absorption coefficient of the material.

- Dwell time (τ) : This is the time period that the laser illuminates the target aimpoint and is given in units of seconds (s).

4.1.1 Melting

Melting a target involves heating the target to its melting point and continuing to heat it until a hole is melted. Peak irradiance, spot size, target absorptivity, target thickness, and thermal losses due to conduction and radiation must be considered to make melting calculations. Figure 4.1 shows a geometry of a target area exposed to laser irradiation. On the scheme, the laser beam (red) is directed at the target, which causes heating in a circular area of radius r . Heat conduction in the target leads to temperature gradients, shown by the blue arrows, and the thickness of heat penetration is represented by Δz .

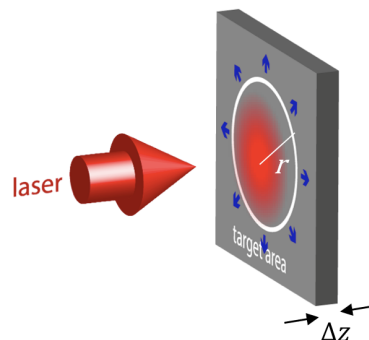


Figure 4.1. Schematic representation of a target area exposed to laser irradiation. Source: [24].

In order to estimate the melt-through time, we must calculate the required energy and account for thermal losses due to conduction and radiation, as detailed in [24]:

- Energy (Q_1) required to reach the melting temperature can be calculated by

$$Q_1 = c_p m \Delta T, \quad (4.3)$$

where c_p is the specific heat capacity of the material, m is the mass of the material that is going to be melted, and ΔT is the change in the temperature.

- Energy (Q_2) required to melt the material at the melting temperature can be calculated by

$$Q_2 = m \Delta H, \quad (4.4)$$

where ΔH is the heat of fusion of the material.

- Thus, the total energy (Q_{melt}) required for melting is then $Q_{melt} = Q_1 + Q_2$.
- Power loss due to radiation is estimated by

$$P_{rad} = \epsilon \sigma A_{rad} \left(T_{melt}^4 - T_0^4 \right), \quad (4.5)$$

where ϵ is the emissivity, σ is the Stefan-Boltzmann constant, T_{melt} is the melting temperature, and T_0 is the ambient temperature. A_{rad} is the area illuminated by the laser and can be calculated as πr^2 , where r is the radius of the illuminated area as depicted in Figure 4.1.

- Power loss due to conduction is estimated as

$$P_{cond} = k A_{cond} (T_{melt} - T_0) / \Delta r, \quad (4.6)$$

where k is the thermal conductivity of target, A_{cond} is the surface area through which the conduction occurs, and can be calculated as $2\pi r \Delta z$, where Δz is the thickness of the heat penetration as depicted in Figure 4.1, and Δr is the distance of a temperature gradient—a transition region with a significant temperature difference. This region typically spans a few centimeters and can be effectively estimated by using thermal cameras [24].

- Total power loss due to radiation and conduction is then $P_{loss} = P_{rad} + P_{cond}$.

To illustrate the calculation of melting time of a 3 mm thick aluminum target, consider the following example in [24] with the parameters given below:

- $A \approx 100 \text{ cm}^2$
- $m \approx 81 \text{ g}$
- $c_p = 900 \text{ J/kg} \cdot \text{K}$
- $T_{melt} = 933 \text{ K}$
- $T_0 = 293 \text{ K}$
- $\Delta H = 4 \cdot 10^5 \text{ J/kg}$
- $P_{abs} = 15 \text{ kW}$ absorbed by the target after atmospheric losses and reflected power (with atmospheric losses of 50% and a reflectivity of 0.7 assumed)
- $P_{loss} = P_{rad} + P_{cond} \approx 3 \text{ kW}$.

Now, we proceed with the calculation by applying these parameters to the formulas given above. First, we calculate the energy required for melting, Q_{melt} , which is approximately 81 kJ. Then the dwell time (τ) required for melting is given by

$$\tau \approx \frac{Q_{melt}}{P_{abs} - P_{loss}} = \frac{81 \text{ kJ}}{15 \text{ kW} - 3 \text{ kW}} = \frac{81 \text{ kJ}}{12 \text{ kJ/s}} \approx 7 \text{ s.}$$

Consequently, in order to melt through a 3 mm thick aluminum target, approximately 7 seconds are required given the parameters above.

4.2 Torvik's Model for Predicting Melt-Through Times

Peter Torvik's model, as proposed in [25], provides a detailed methodology for predicting the melt-through times due to exposure to HEL irradiation for various relevant materials. The model employs fundamental heat transfer equations, considering factors like material thermal properties, laser power, and target thickness. In contrast to the equations used in the previous section, which rely on more simplified approaches, Peter Torvik developed a model that provides a more sophisticated and comprehensive framework. This model is validated with experimental results, ensuring greater accuracy and reliability in predicting melt-through times. One of the significant assumptions of the model is that the melted part

is removed as soon as it is created. It also assumes that all of the properties are temperature independent.

4.2.1 Variables of the Model

Key variables of the model are as follows [25]:

- The minimum melt-through time (t_I) is the melt-through time that assumes heat only propagates axially, through the thickness, neglecting any radial heat transfer. It can be estimated by

$$t_I = \frac{\rho l}{\alpha I} [c_p (T_m - T_0) + \Delta H], \quad (4.7)$$

where ρ is the density of the material, l is the thickness, α is the absorption coefficient (1 – Reflectivity) of the material, I is the irradiance, c_p is the specific heat, T_m is the melting temperature, T_0 is the ambient temperature, and ΔH is the latent heat of fusion.

- The dimensionless melting time (θ) is the ratio of actual melting time (t_m) to minimum melting time (t_I). It provides an insight of the directionality of the heat propagation. Large θ values indicate that heat is transferred more radially than axially.
- Absorbed power (P_{abs}) is the power absorbed by the target and can be estimated by

$$P_{abs} = \alpha I \pi w_{tot}^2, \quad (4.8)$$

where w_{tot} is the spot size radius.

- Dimensionless absorbed power per unit thickness (P_{la}) is another indicator of the directionality of the heat transfer and can be calculated by

$$P_{la} = \frac{P_{abs}}{l \kappa \rho [\Delta H + c_p (T_m - T_0)]}, \quad (4.9)$$

where κ is the thermal diffusivity [25]

4.2.2 Estimation of Melt-Through Times

Figure 4.2 shows the computed results, which were obtained from [26] for different materials using the numerical method proposed in [27] with the assumption of melt removal. The

symbols represent the actual data for the corresponding materials, while the fitting curve serves as a tool for estimating the melt-through times of the relevant materials. Once the dimensionless absorbed power per unit length is calculated, the actual melt-through time can be simply calculated by the product of the minimum melting time and the dimensionless melting time. The plot was generated by manually picking data points from [25], and a spline fit was implemented to create the curve.

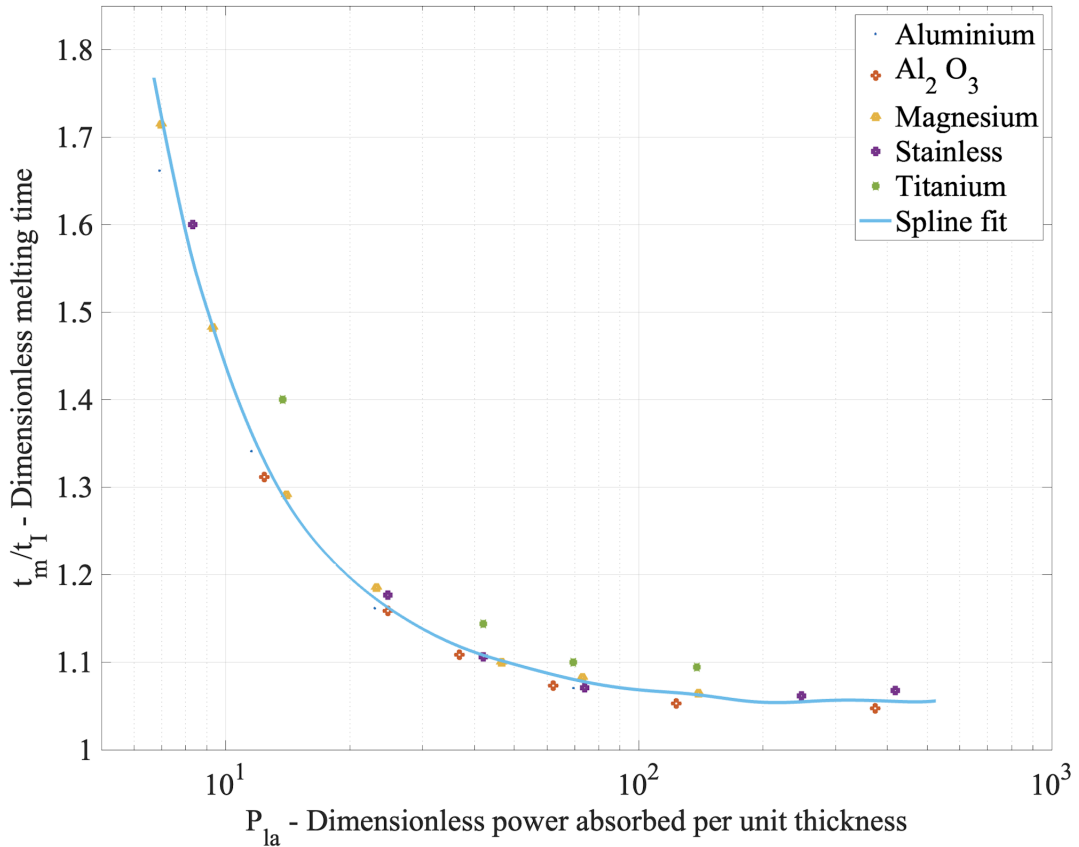


Figure 4.2. Dimensionless melting time as a function of dimensionless absorbed power per unit length. Adapted from [25].

4.2.3 Validation of the Model

In order to validate that the Torvik's model was implemented properly, estimated melt-through times were calculated by using both the rough calculations made in Section 4.1, and Torvik's model were compared in Figure 4.3 and Figure 4.4 for two different materials.

A spot size of 100 cm^2 and an absorption coefficient of 0.3 were assumed for both targets. Figure 4.3 shows the melting times as a function of power for a 3 mm thick aluminum target. The red line represents the minimum melting time, which does not account for the radial heat losses, calculated by using Torvik's model. As expected, it turned out to be the minimum melting time among the three. The blue line represents the melting time calculated by the approximate calculations in Section 4.1, which turned out to be the maximum melt-through time. The yellow line represents the actual melt-through times estimated by Torvik's model, which lies between the two melt-through times. As the power increases, the differences among these three melt-through times decrease. This is because at high powers, the loss mechanism becomes less important.

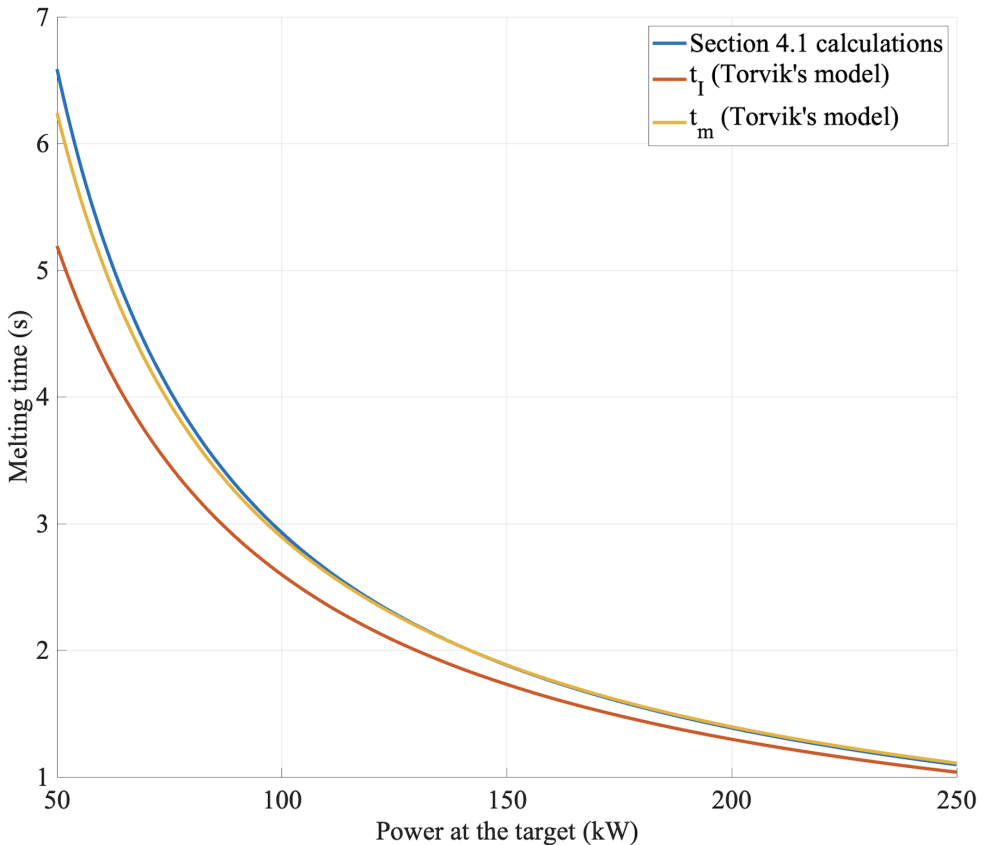


Figure 4.3. Comparison of three melt-through times for the 3 mm thick aluminum target as a function of the power arrives at the target.

The above-mentioned considerations imply that the implementation of the model is successful and the actual melt-through times are realistic. Figure 4.4 shows the melting times as a function of power for a 10 mm thick stainless-steel target. All the conclusions mentioned in Figure 4.3 are also valid for Figure 4.4.

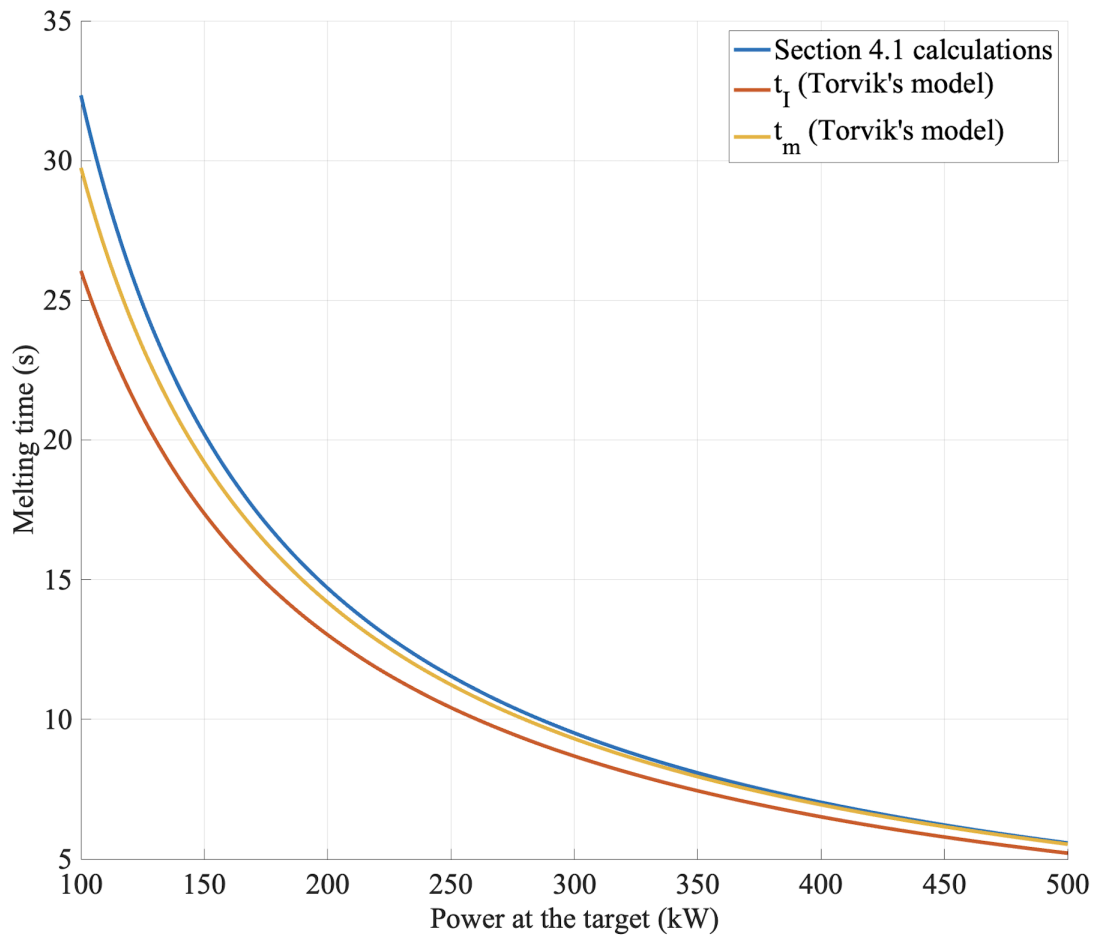


Figure 4.4. Comparison of three melt-through times for the 10 mm thick stainless-steel target as a function of the power arrives at the target.

CHAPTER 5: Simulation Parameters and Results

This chapter presents the simulation parameters and results for evaluating HEL effectiveness in the Mediterranean maritime environment. It covers selected points with their turbulence profiles, target types and their material properties, laser parameters, and a sensitivity analysis of factors like laser power, engagement distance, target thickness, and target altitude.

5.1 Mediterranean Maritime Environment

The atmospheric profiles used in this thesis were provided by Paul Frederickson from the NPS Department of Meteorology. He developed two models to generate C_n^2 profiles for a particular area [28]:

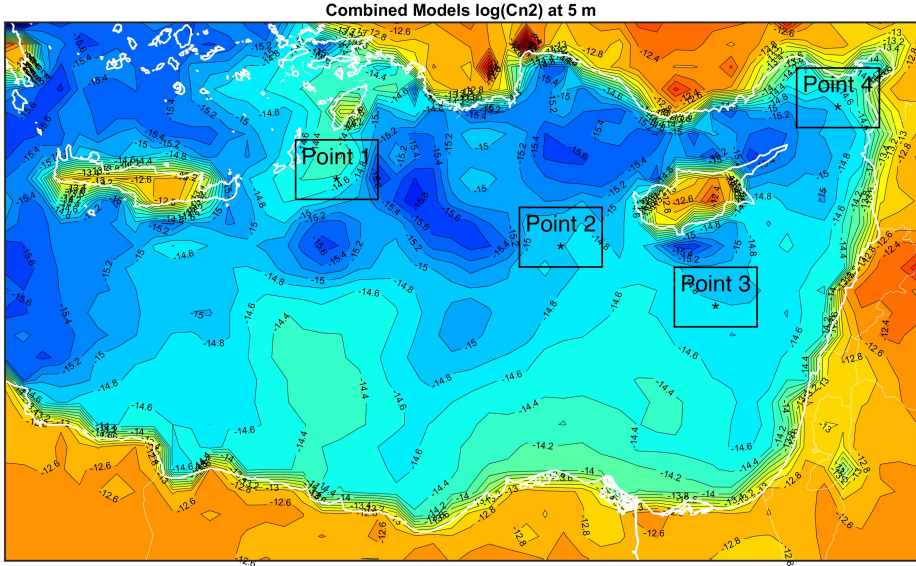
- The Navy Atmospheric Vertical Surface Layer Model (NAVSLaM) is used to model vertical profiles close to the surface of the Earth, within the range of 0-100 m.
- The Tropospheric Optical Turbulence Ensemble of Models (TOTEM) is used to model upper-air profiles.

These two models are integrated using the Profile Blending Algorithm (Cn2PBA) to create comprehensive C_n^2 profiles [28]. Data from ERA5 was utilized in these models [29].

Figure 5.1 shows the C_n^2 profile at 5 meters in the Mediterranean Sea, computed by NAVS-LaM using data from ERA5 for 12Z on September 1, 2017 [28]. The blue color corresponds to regions of mild turbulence, while the red indicates areas of severe turbulence. Four locations, marked with asterisks in Figure 5.1, were selected to represent a diverse range of geographical locations. Turbulence profiles for these locations were generated across four different seasons and at four different times of the day, with six-hour intervals to provide a comprehensive understanding of the atmospheric conditions in the region.

Frederickson provided the datasets at 11 percentiles (1st, 5th, 10th, 25th, 40th, 50th, 60th, 75th, 90th, 95th, and 99th) to illustrate the variations in turbulence profiles. Figure 5.2 shows a box plot of the C_n^2 values at a height of 5 meters, categorized by different seasons and times of day. The bottom edge of each box corresponds to the 25th percentile, the red

line within the box represents the median or 50th percentile, and the top edge of the box indicates the 75th percentile; outliers are represented by horizontal black lines. The C_n^2 values are plotted on a logarithmic scale with base 10, where more negative values on the y-axis indicate weaker turbulence.



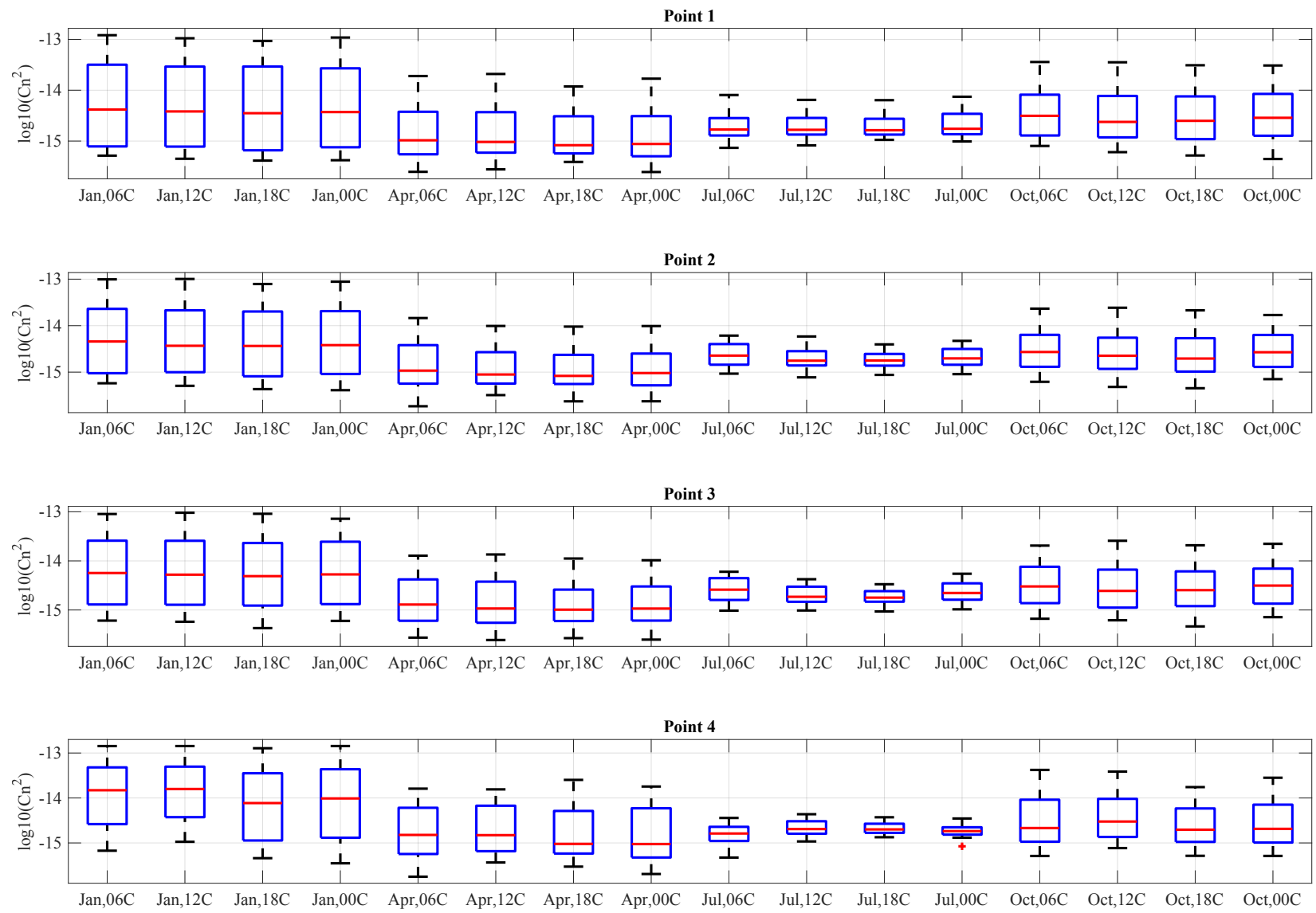


Figure 5.2. Seasonal and daytime variations of the C_n^2 at 5 meters above the surface.

Figure 5.3 shows the vertical turbulence profiles up to an altitude of 3000 m for different seasons at specific points. The profiles illustrate seasonal variations in vertical turbulence profiles, with blue representing winter, yellow representing summer, red representing spring, and purple representing fall. The x-axis represents the log base 10 of C_n^2 values, where more negative values indicate milder turbulence, while the y-axis depicts the altitude in a logarithmic scale. The figure represents the median values for the 09Z time and suggests that turbulence generally decreases with altitude up to a point, after which it increases before declining again. Notably, the winter season's trend change occurs at higher altitudes compared to other seasons. Additionally, at Point 4, the decrease in turbulence during the winter season is less pronounced compared to the other points.

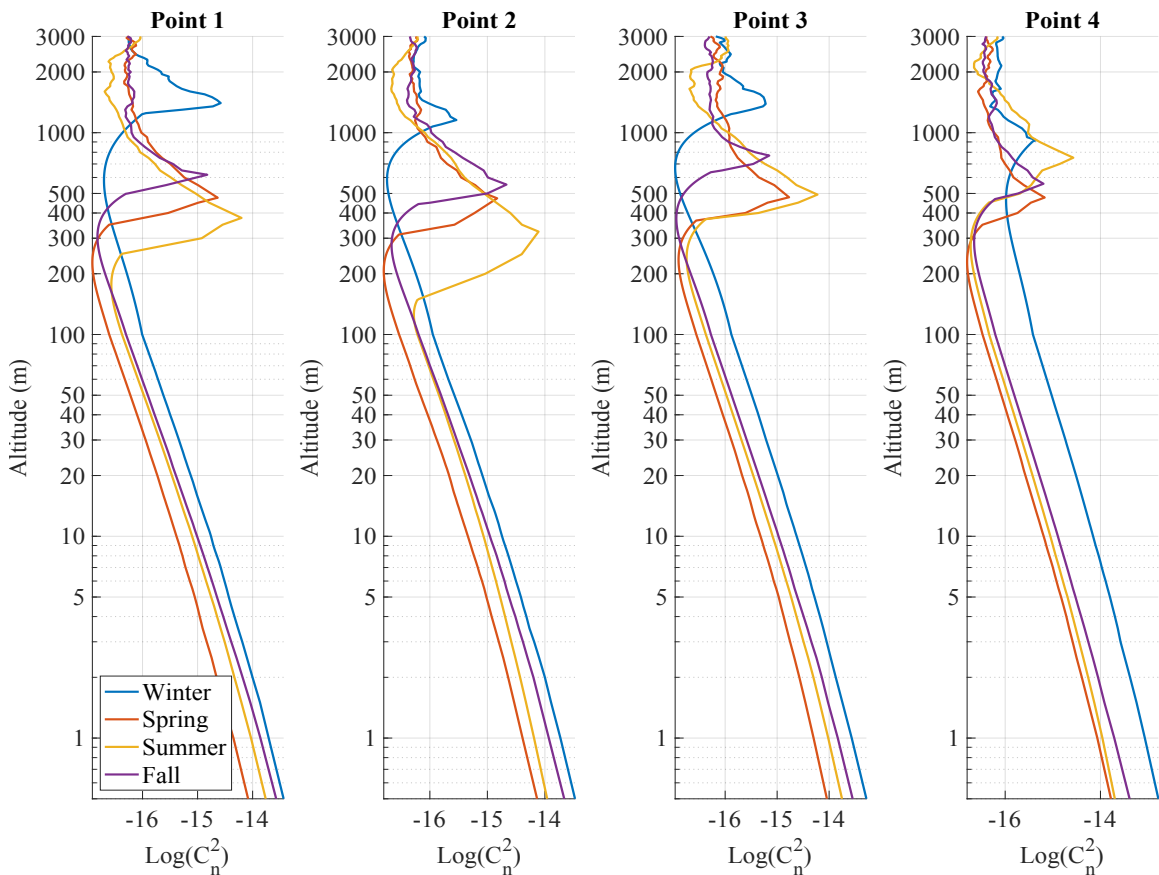


Figure 5.3. Vertical turbulence profiles up to 3000 m across different seasons at four specific points in the Mediterranean region, based on median values at 09Z time.

5.2 Simulation Parameters

C_n^2 profiles were obtained from NAVSLaM and TOTEM, covering altitudes ranging from 0 to 3000 meters. Although C_n^2 varies significantly with height, it exhibits minimal variation in the horizontal direction. Consequently, lateral C_n^2 profiles were assumed to be constant over a range of 5000 meters from each point. The altitude was linearly varied from the platform height to the target height along the path, and the corresponding C_n^2 values for each altitude were used in this thesis.

The number of phase screens significantly impacts the computational effort. To optimize performance, the number of phase screens was dynamically adjusted in each simulation to ensure that only the minimum number necessary to accurately capture the turbulence effects was used. The adjustment was based on the highest C_n^2 values encountered along the path during each iteration. This minimum number refers to the point beyond which adding more does not improve accuracy but only increases computational time. Thus, this approach significantly reduced computational time without compromising accuracy. The other simulation parameters are presented in Table 5.1.

Table 5.1. Parameters used in the simulation.

Parameter	Value
Laser wavelength	1 μm
Output power	100 kW
Beam director radius	0.1 m
Target distance	5000 m
Platform height	5 m
Number of grid points	1024
Extinction coefficient	10^{-4} m^{-1}
Number of realizations	128
Reflection coefficient	0.3

5.3 Target Types and Material Properties

Various target types, including both surface and aerial targets, were analyzed. Table 5.2 presents the different target types along with their corresponding material properties and the assumptions applied in the analysis.

Table 5.2. Target material properties and assumptions. Adapted from [30]–[32].

Target	Assumed Material	Assumed Thickness (mm)	Assumed Altitude (m)	Density (g/cm ³)	Specific Heat (J/KgK)	Thermal Conductivity (W/mK)	Melting Temperature (K)	Heat of Fusion (kJ/kg)
Reconnaissance Drone	Aluminum 7075-T6	2	3000	3	870	130	913	380
Helicopter	Aluminum 7075-T6	6	3000	3	870	130	913	380
Missile	Ti-6Al-4V (Grade 5)	5	3000	4.4	560	6.8	1883	410
Patrol Boat Hull	Aluminum 7075-T6	10	1	3	870	130	913	380
Radar Antenna	304 Stainless Steel	8	30	7.8	480	16	1723	290
Cargo Container	304 Stainless Steel	2	1	7.8	480	16	1723	290
Floating Mine	304 Stainless Steel	10	1	7.8	480	16	1723	290
Amphibious Vehicle	Aluminum 7075-T6	8	1	3	870	130	913	380

5.4 Results

The results of the laser engagement simulations are categorized into surface and aerial targets. For each target and season, the 25th, 50th, and 75th percentile C_n^2 profiles were used to determine the required time for melt-through. The 25th percentile represents favorable conditions, the 50th percentile reflects median conditions, and the 75th percentile corresponds to cases with stronger turbulence.

5.4.1 Surface Engagements

The results of laser engagements with a range of surface targets, including patrol boat hulls, radar antennas, cargo containers, floating mines, and amphibious vehicles, were analyzed. Figures 5.4-5.8 show the predicted melt-through times for surface targets across four different points in the Mediterranean Sea. Each subplot corresponds to one of these points (labeled as Point 1, Point 2, Point 3, and Point 4). The melt-through times are shown on the vertical axis in logarithmic scale (measured in seconds), while the horizontal axis represents the four seasons (Winter, Spring, Summer, and Fall). Each box plot within a subplot shows the range of melt-through times for three different percentile profiles (25th, 50th, and 75th percentiles) of the C_n^2 profiles.

The blue boxes represent the middle 50% of the data. The red lines within the boxes represent the median melt-through time for each season.

Key observations from the results is as follows:

- The melt-through times vary significantly across different points, with Point 4 demonstrating the highest melt-through times.
- Certain seasons, particularly winter, show a broad spread in melt-through times, indicating greater variability in atmospheric conditions.
- The summer season is characterized by the narrowest spread in melt-through times, indicating lower variability in atmospheric conditions.
- Across all points, the spring season consistently allows for the minimum melt-through times.

5.4.1.1 Patrol Boat Hull

Figure 5.4 shows the predicted melt-through times for a patrol boat hull, which was assumed to be made of 10 mm thick aluminum. Under optimal conditions, specifically during a spring day, melt-through times of less than 15 seconds are observed across all four points. For all points, except during the winter season, median melt-through times remain under 55 seconds. Winter season displays the broader spread in melt-through times. Particularly at Point 4, winter melt-through times can extend up to 650 seconds, which may not be operationally feasible.

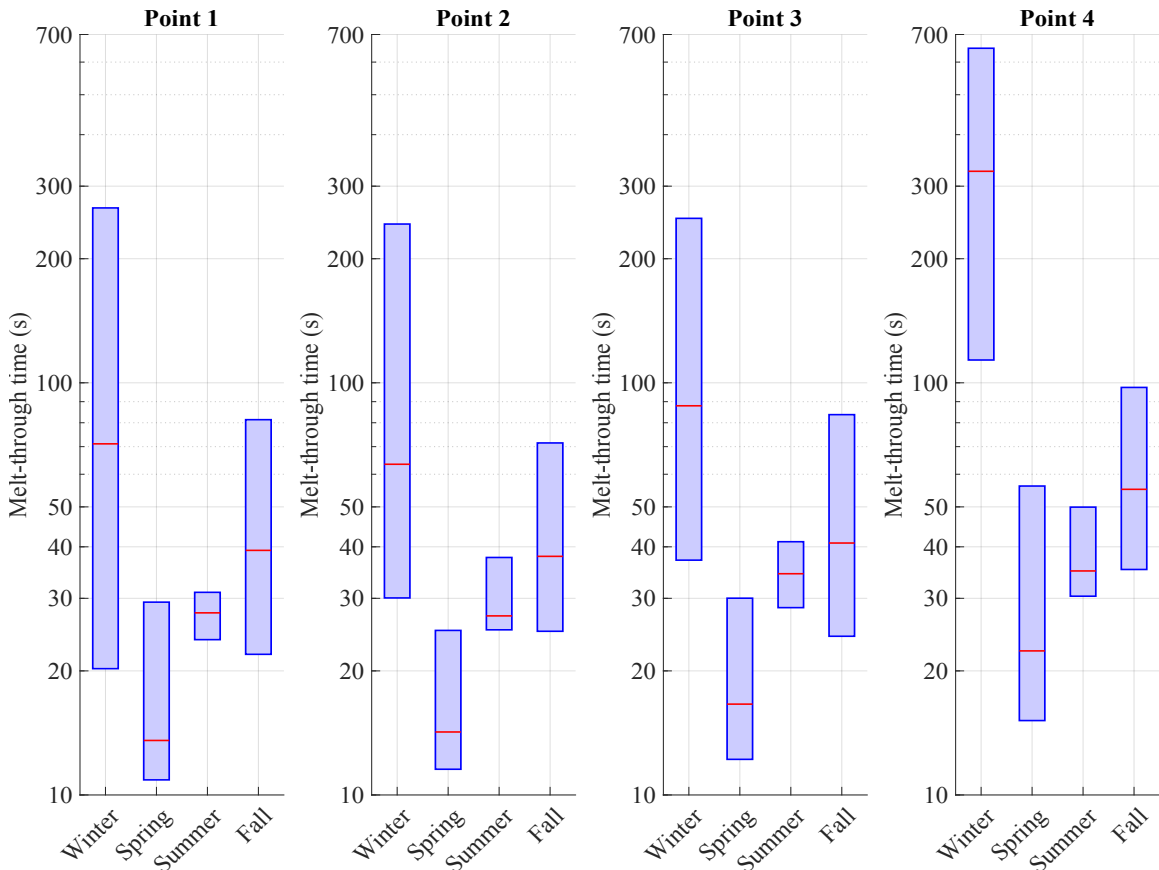


Figure 5.4. Predicted melt-through times for a patrol boat hull at four points in the Mediterranean Sea, showing variability across seasons for the 25th, 50th, and 75th percentile C_n^2 profiles.

5.4.1.2 Radar Antenna

Figure 5.5 illustrates the predicted melt-through times for a radar antenna, which was assumed to be made of 8 mm thick stainless steel. Under optimal conditions, specifically during a spring day, melt-through times of less than 6 seconds are achieved across all four points. For all points, except during the winter season, median melt-through times remain under 17 seconds. Winter season display the broader spread in melt-through times. However, even in the worst-case scenarios, except for Point 4, melt-through times during winter remain below 80 seconds, which may be considered operationally favorable. The radar antenna's melt-through times are lower compared to the patrol boat hull mainly due to its 30-meter altitude, which reduces turbulence effects significantly compared to sea level. Targeting a radar antenna at Point 4 during the winter season may require further evaluation, as the melt-through time extends to 200 seconds.

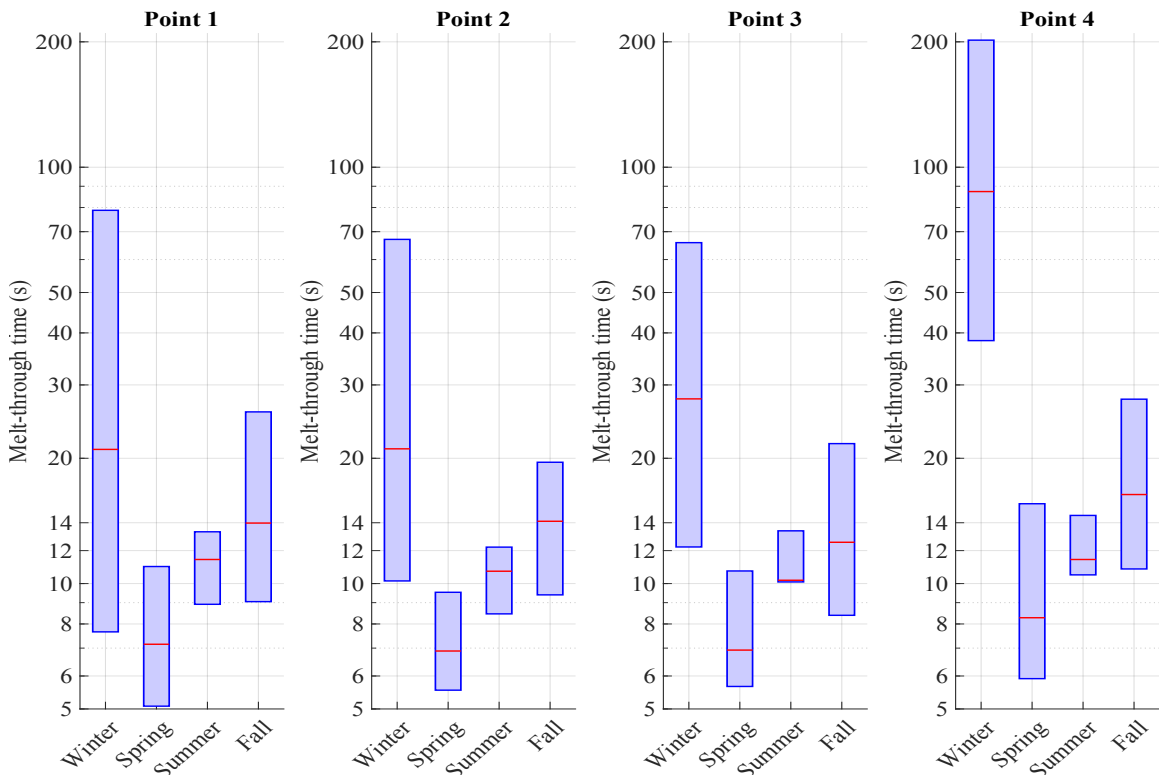


Figure 5.5. Predicted melt-through times for a radar antenna at four points in the Mediterranean Sea, showing variability across seasons for the 25th, 50th, and 75th percentile C_n^2 profiles.

5.4.1.3 Cargo Container

Figure 5.6 illustrates the predicted melt-through times for a cargo container, which was assumed to be made of 2 mm thick stainless steel. Under optimal conditions, specifically during a spring day, melt-through times of less than 4 seconds are achieved across all four points. Except during the winter season, even in the worst-case scenarios, melt-through times at all points remain under 20 seconds. During winter, the worst-case melt-through times remain below 60 seconds, except at Point 4, where the melt-through time extends up to 160 seconds.

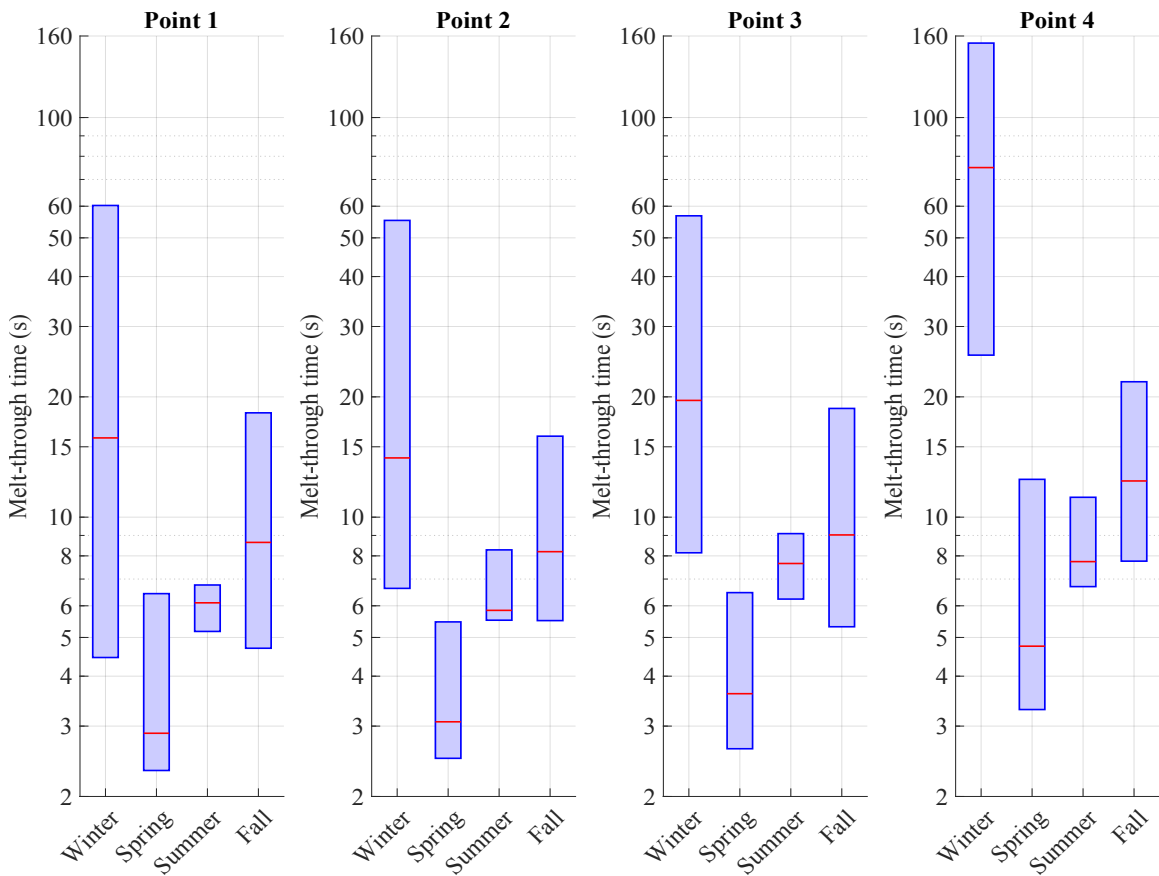


Figure 5.6. Predicted melt-through times for a cargo container at four points in the Mediterranean Sea, showing variability across seasons for the 25th, 50th, and 75th percentile C_n^2 profiles.

5.4.1.4 Floating Mine

Figure 5.7 illustrates the predicted melt-through times for a floating mine, which was assumed to be made of 10 mm thick stainless steel. Under optimal conditions, specifically during a spring day, melt-through times of less than 20 seconds are achieved across all four points. For all points, except during the winter season, median melt-through times remain under 65 seconds. Winter season display the broader spread in melt-through times. Particularly at Point 4, winter melt-through times can extend up to 800 seconds. However, given that the mine is floating, the extended melt-through time may not undermine the efficacy of HELs. Even if they have long melt-through durations, HELs could still represent a reasonable and effective option for neutralizing floating mines.

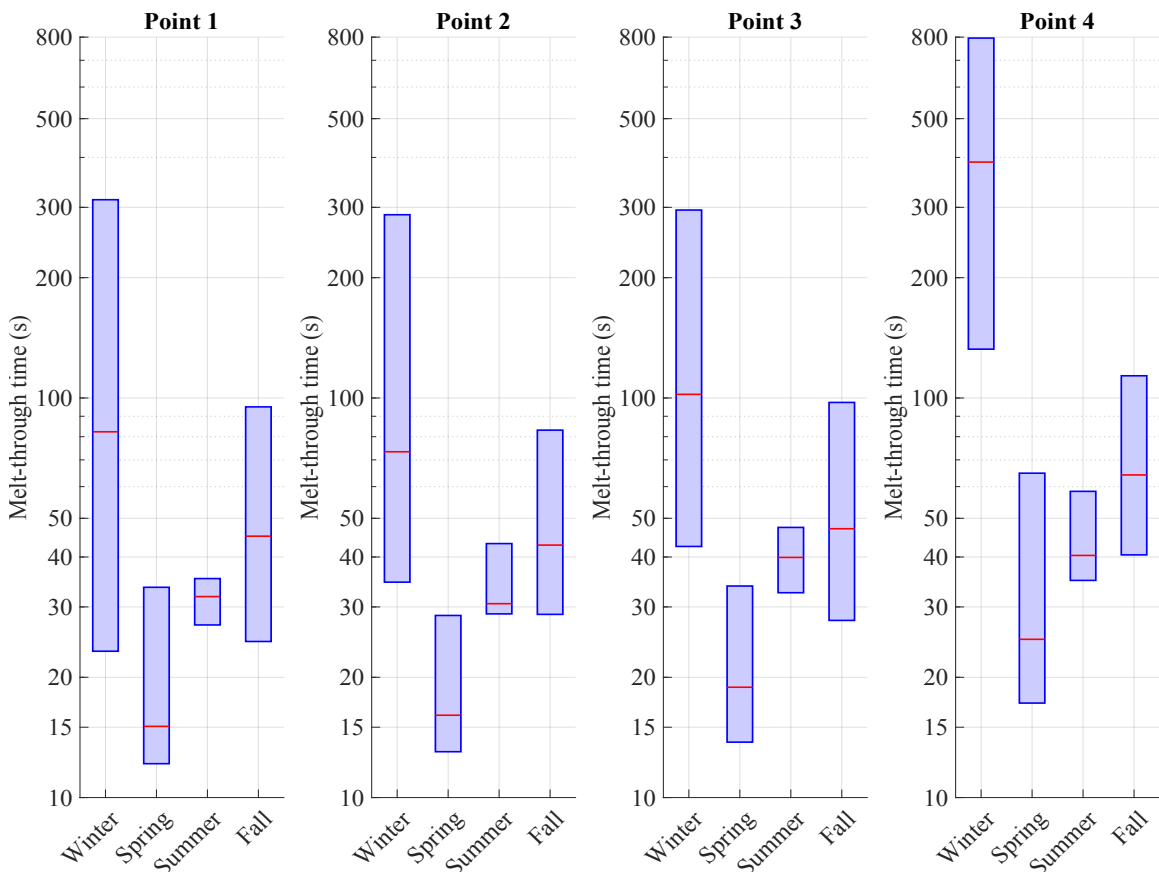


Figure 5.7. Predicted melt-through times for a floating mine at four points in the Mediterranean Sea, showing variability across seasons for the 25th, 50th, and 75th percentile C_n^2 profiles.

5.4.1.5 Amphibious Vehicle

Figure 5.8 illustrates the predicted melt-through times for an amphibious vehicle, which was assumed to be made of 8 mm thick aluminum. Under optimal conditions, specifically during a spring day, melt-through times of less than 6 seconds are achieved across all four points. For all points, except during the winter season, median melt-through times remain under 22 seconds. Winter season display the broader spread in melt-through times. During winter, the worst-case melt-through times remain below 100 seconds, except at Point 4, where the melt-through time extends up to 270 seconds.

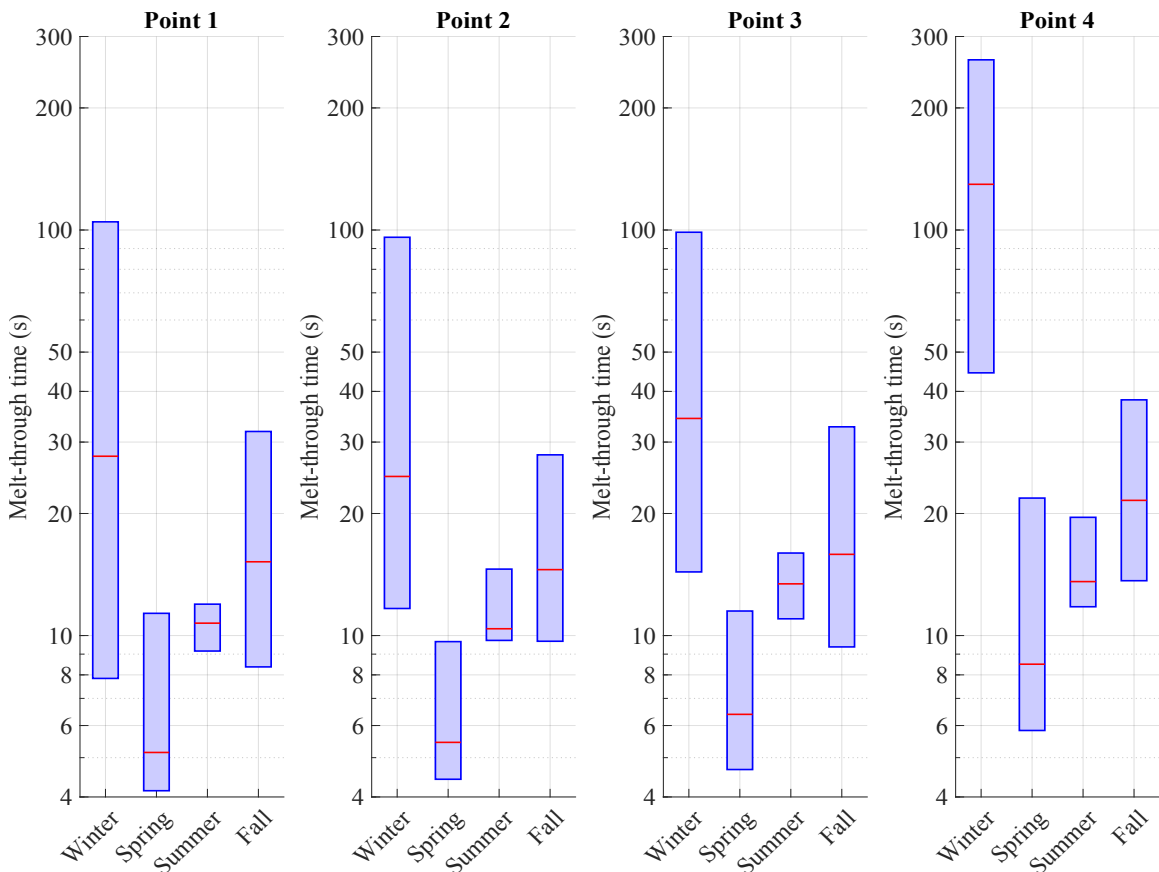


Figure 5.8. Predicted melt-through times for an amphibious vehicle at four points in the Mediterranean Sea, showing variability across seasons for the 25th, 50th, and 75th percentile C_n^2 profiles.

5.4.2 Aerial Engagements

The results of laser engagements with a range of aerial targets (cf. Table 5.2), including reconnaissance drone, helicopter, and missile, were analyzed. Figure 5.9 presents the predicted melt-through times for these aerial targets across four seasons at specific points in the Mediterranean Sea, with blue representing the reconnaissance drone, yellow representing the helicopter, and red representing the missile. The melt-through times are based on the median values at 09Z time. All targets exhibit melt-through times below 5 seconds, with the drone consistently yielding times of less than one second. This suggests that aerial engagements result in significantly shorter melt-through times compared to surface engagements, highlighting the decreased turbulence effect at higher altitudes. Notably, the summer season at Point 2 and the winter season at Point 4 show a marked increase in melt-through times. This is because, in Point 2 during the summer, as shown in Figure 5.3, the turbulence profile undergoes a significant shift around an altitude of 150 meters, leading to prolonged exposure to more severe turbulence. Similarly, in Point 4 during the winter, the turbulence profile remains relatively severe compared to other seasons, resulting in less favorable conditions for laser propagation and, consequently, longer melt-through times.

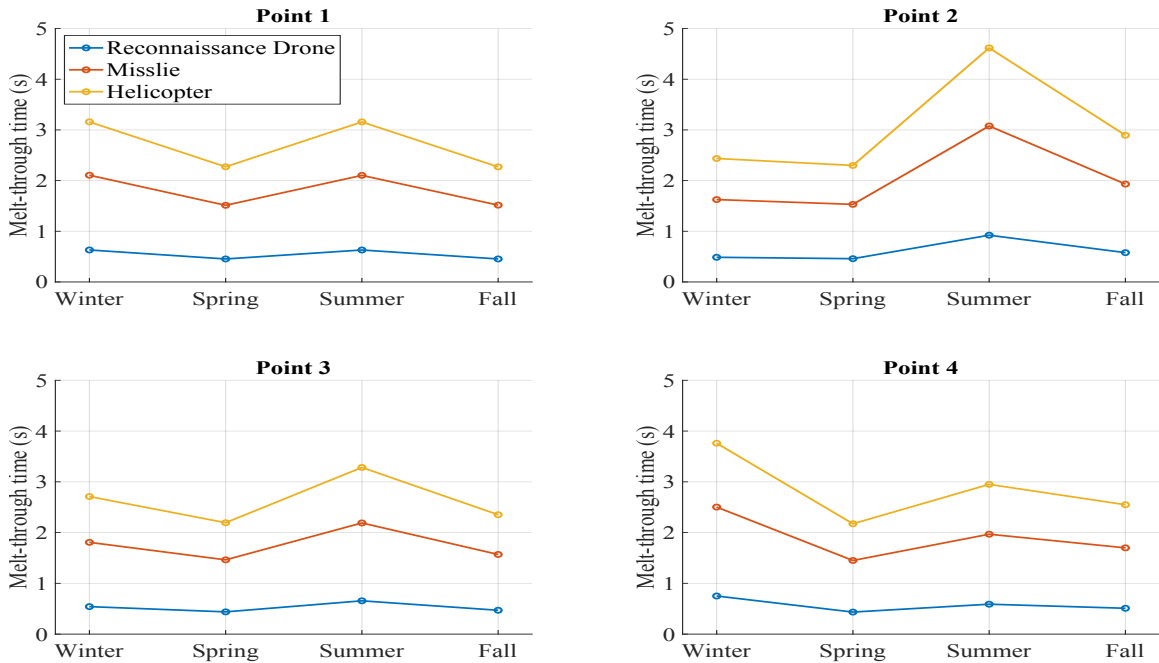


Figure 5.9. Predicted melt-through times for aerial targets across four seasons at four specific points, based on the median values at 09Z time.

5.5 Sensitivity Analysis

The sensitivity of melt-through times to various key parameters, including laser output power, range, target thickness, and target height was examined to provide a comprehensive understanding of their influence on the effectiveness of HELs. All parameters used in the sensitivity analysis are as defined in Section 5.2, except for the parameters whose sensitivity is analyzed.

5.5.1 Sensitivity to Laser Output Power and Range

Figure 5.10 shows the sensitivity of melt-through time for a patrol boat hull to varying laser output power and engagement ranges across the four seasons at Point 1. Laser output power ranged from 10 kW to 100 kW, while the engagement distance varied from 500 meters to 5000 meters. The SLM was used in this analysis to provide an overview, as only the median C_n^2 values were considered, with the understanding that real-life atmospheric variations could lead to different results.

The colors in the figure represent different melt-through time ranges corresponding to the given power and distance parameters. The blue zone indicates a melt-through time of less than 10 seconds, which could be operationally advantageous depending on mission requirements, while the red zone represents a melt-through time of greater than 90 seconds, which may introduce operational challenges. The other melt-through time ranges are displayed in the color bar.

As noted in the previous section, the winter season exhibits the most fluctuations in the turbulence profile, resulting in the longest melt-through times. However, the results for winter and fall appear similar because the median C_n^2 values for these seasons are very close to each other. Figure 5.10 serves as a quick reference tool for estimating the melt-through time of a patrol boat hull based on specific output power and distance parameters around Point 1.

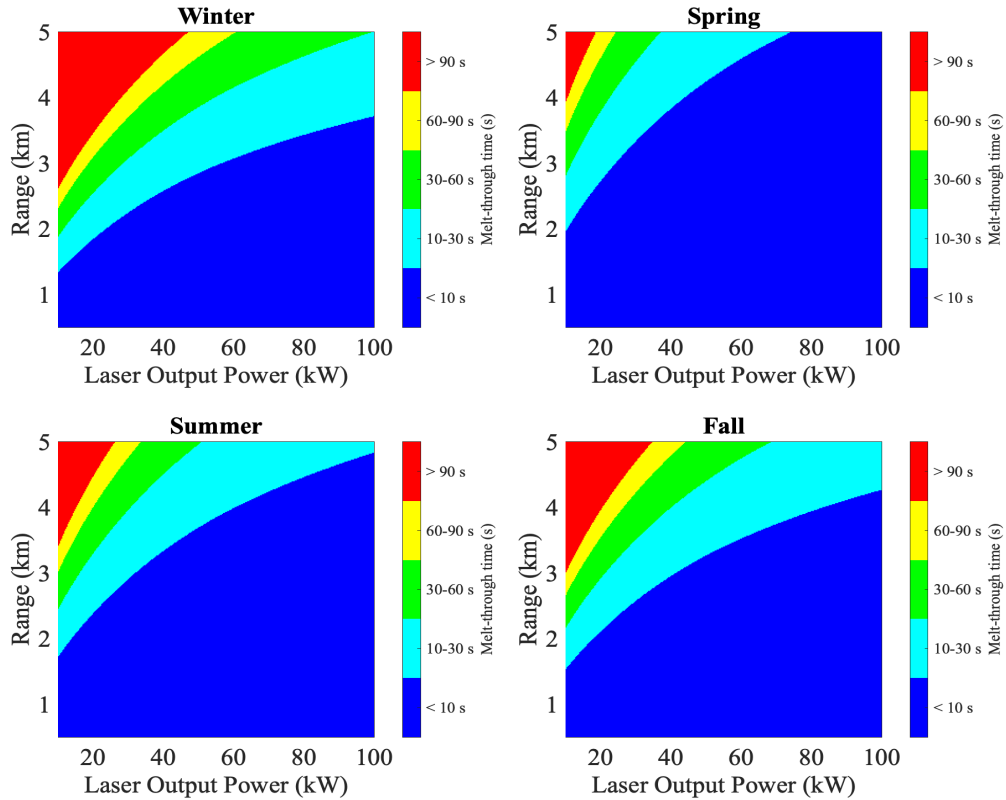


Figure 5.10. Sensitivity of melt-through time for a patrol boat hull to varying laser output power and range across different seasons at Point 1.

5.5.2 Sensitivity to Target Thickness

Figure 5.11 shows the sensitivity of melt-through time to aluminum target thickness across four seasons at four specific points. The target thickness varied from 1 mm to 10 mm, and the median irradiance and spot size values, calculated by FDM, were used to estimate the melt-through time corresponding to each thickness. To highlight key results, the melt-through time scale is limited to 60 seconds. As shown in Figure 5.11, at Point 4 during the winter season, a melt-through time of 60 seconds is achieved with a 4 mm thickness, which exceeds the scale limit. Apart from the winter results at Point 4, the melt-through times are similar across the other points. This figure can be used as a reference for estimating melt-through times for an aluminum target up to 10 mm thick across all seasons and at four points.

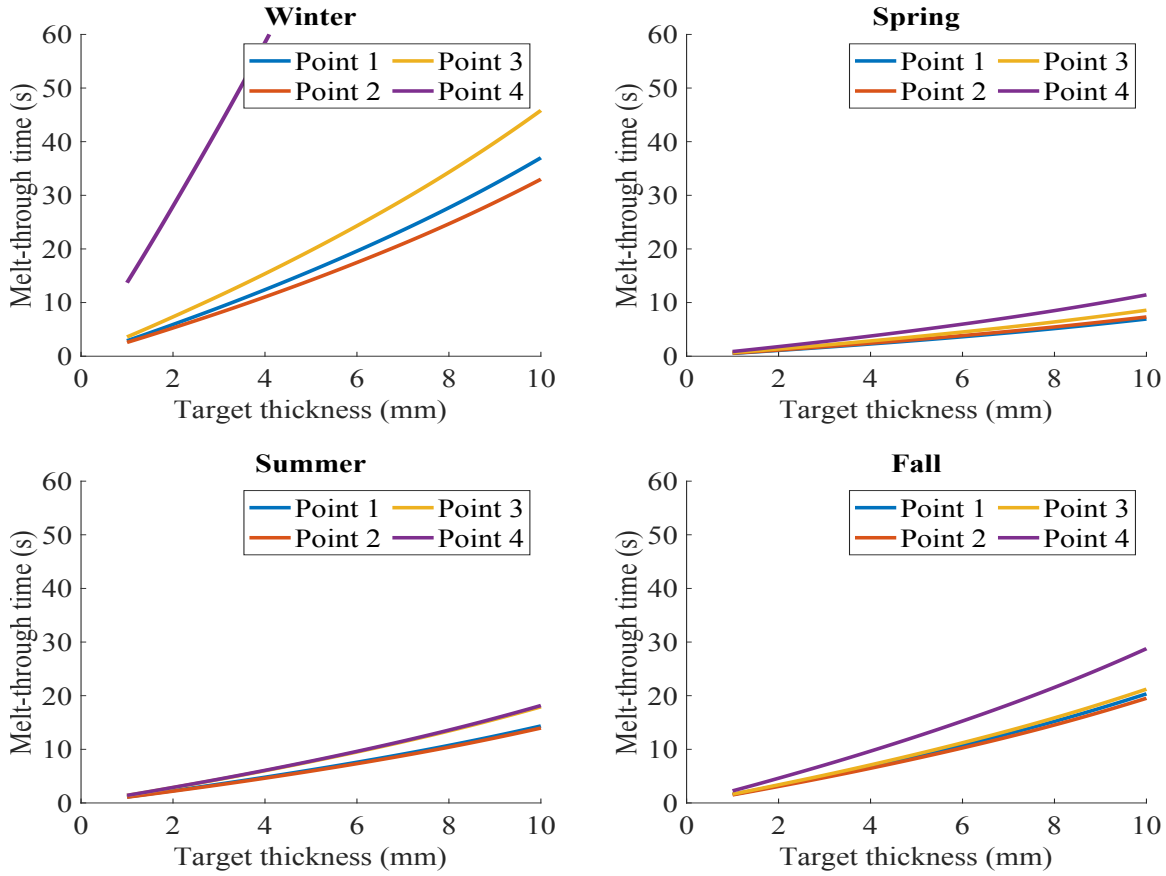


Figure 5.11. Sensitivity of melt-through time to aluminum target thickness across four seasons at four specific points.

5.5.3 Sensitivity to Target Altitude

Figure 5.12 shows the sensitivity of percentage decrease in melt-through time for a radar antenna with respect to a reference height of 5 m. This effort is done for illustrating how sensitive the melt-through time to the target altitude. Target altitude varied from 5 meters to 30 meters. The melt-through time at 5 meters is assumed to be the reference and the percentage decrease in melt-through time for each altitude is calculated and plotted on the y-axis. The SLM was used in this analysis to provide an overview, as only the median C_n^2 values were considered, with the understanding that real-life atmospheric variations could lead to different results.

As the target altitude increases, there is a consistent decrease in melt-through time across all seasons and four points. Although all points exhibit a similar decreasing trend, Point 2 shows the minimum percentage decrease compared to the others. This might suggest that the specific turbulence profile at Point 2 makes it less sensitive to altitude changes.

Even for 25 meters increase in altitude, a significant decrease in melt-through time is evident (ranging from 40% to 60%), highlighting the strong influence of altitude on laser effectiveness.

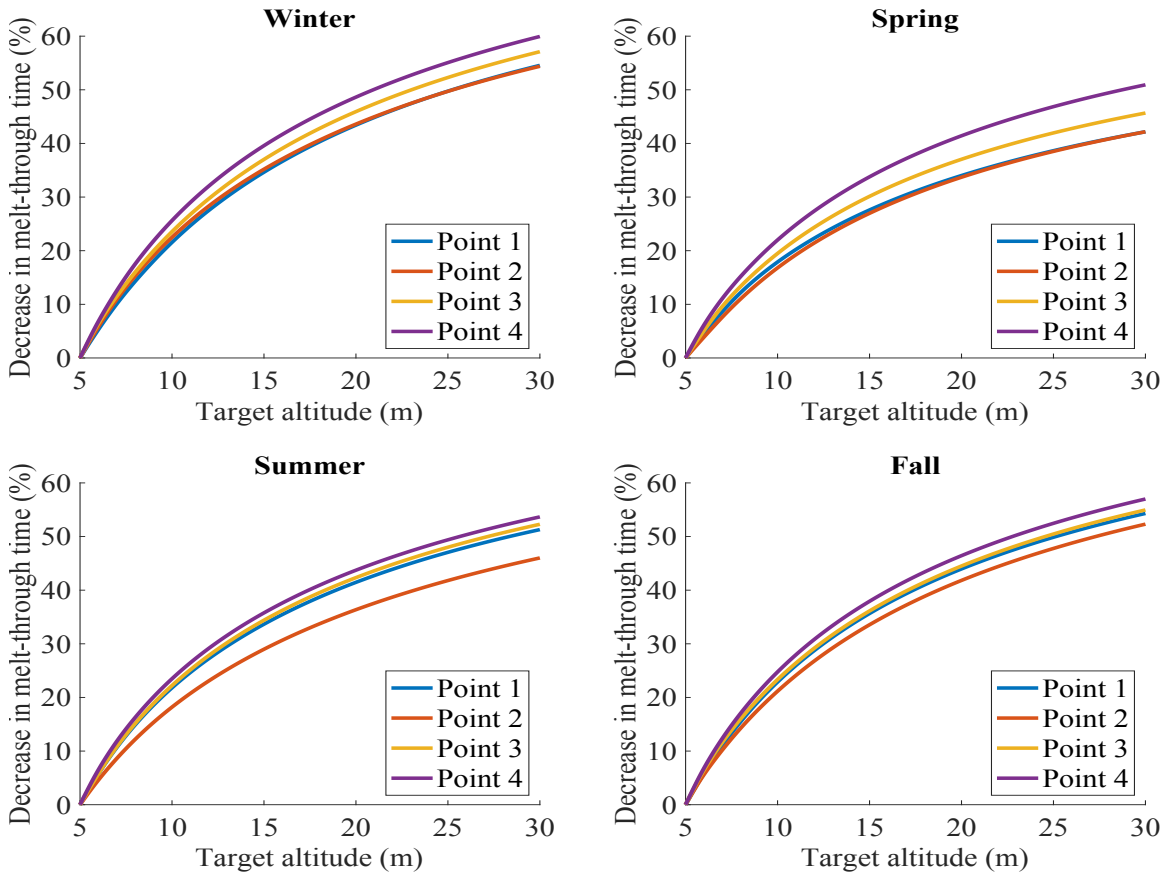


Figure 5.12. Sensitivity of melt-through time to target altitude across four seasons at four specific points, showing the percentage decrease in melt-through time relative to a 5-meter reference height for a radar antenna.

THIS PAGE INTENTIONALLY LEFT BLANK

CHAPTER 6: Conclusion

This thesis examined the effectiveness of HELs in the Mediterranean maritime environment. Atmospheric propagation and lethality were assessed under varying atmospheric conditions across multiple engagement scenarios. The study was conducted through a comprehensive analysis that included theoretical foundations, numerical modeling, and simulation results. The research provided a detailed understanding of the operational capabilities and limitations of HEL systems in the Mediterranean maritime environment.

6.1 Summary of Findings

The analysis began by examining the fundamental physics of laser beam propagation, with a particular emphasis on the Mediterranean's atmospheric conditions. The main focus was to identify the effect of turbulence on HEL performance. Turbulence, especially in the lower atmosphere, was found to be a critical factor that could significantly affect the laser's effectiveness and reduce the irradiance reaching the target. Four points in the Mediterranean environment were selected to capture the impact of different turbulence profiles.

To simulate laser beam propagation, the SLM and the FDM were employed. The SLM provided rapid predictions of time-averaged irradiance at the target with a reasonable accuracy. In contrast, the FDM offered more precise results but required greater computational effort. The FDM was particularly superior for scenarios where turbulence varied along the beam path.

The thesis also focused on the lethality of HELs by estimating melt-through times for various target materials using Peter Torvik's model. The analysis was made considering the energy required to melt-through targets of different material properties and thicknesses. Results showed that melt-through times are highly sensitive to laser output power, target material properties, and atmospheric conditions. The sensitivity analysis revealed that even small variations in these parameters could cause observable changes in the effectiveness of the HEL system.

The research demonstrated that, under favorable conditions, HELs can serve as powerful tools for maritime defense. HELs are capable of neutralizing a wide range of threats, including aerial drones, missiles, and small surface targets. However, the effectiveness of these systems is not guaranteed under all conditions. For instance, in scenarios where turbulence is particularly strong, the effectiveness of HELs could significantly diminish.

6.2 Future Research

There are several areas for future research that build on the findings of this thesis. First, since this study utilized static atmospheric profiles, there is a need to integrate real-time atmospheric data into the models to achieve more accurate predictions. Additionally, as the extinction coefficient was held constant in this thesis, employing more accurate extinction coefficient values could yield more realistic results. Finally, the lethality model could be refined, as it significantly impacts the overall accuracy of the evaluations.

APPENDIX A: Auxiliary Functions for MATLAB Implementation

The MATLAB functions are adapted from [14], [23].

```
1 function [ Etot ,X,Y] = fresnel_conv(E0 ,lambda ,Ws,W,z)
2 % E0 = complex field at source plane (2D matrix)
3 % lambda = wavelength
4 % Ws = width of source grid E0
5 % W = width of target grid E0
6 % z = target screen distance from source
7 % Etot = complex field at target (2D matrix)
8 % X,Y = 2D coordinates at target (2D matrix)
9
10 N = size(E0,1); % # of grid points , each dimension
11 if mod(N,2)==1
12     disp('Make sure N is even for best results!');
13 end
14 k = 2*pi/lambda; % wavenumber
15 M = W/Ws; % scaling parameter
16
17 % coordinates (source plane)
18 dxs = Ws/N; % grid spacing of source
19 [Xs,Ys] = meshgrid((-N/2:N/2-1)*dxs); % source grid
20 rssq = Xs .^2 + Ys .^2;
21
22 % spatial frequencies (source plane)
23 dfs = 1/Ws;
24 [fXs,fYs] = meshgrid((-N/2:N/2-1)*dfs);
25 fsq = fXs .^2 + fYs .^2;
26
27 % coordinates (target plane)
28 dx = W/N; % grid spacing of target
29 [X,Y] = meshgrid((-N/2:N/2-1) * dx);
```

```

30 rsq = X.^2 + Y.^2;
31
32 % phase factors
33 Q1 = exp(1i*k/2*(1-M)/z*rsq);
34 Q2 = exp(-1i*pi^2*2*z/M/k*fsq);
35 Q3 = exp(1i*k/2*(M-1)/(M*z)*rsq);
36
37 % compute the propagated field
38 Etot = Q3.*ift2D(Q2.*ft2D(Q1.*E0/M,dxs),dfs);
39 end

```

```

1 function phi = phase_screen(Cn2, N, lambda, W, dz)
2 % Cn2 = local turbulence refractive structure parameter
3 % N = grid size of desired phase screen
4 % lambda = laser wavelength
5 % W = transverse window width
6 % dz = propagation distance
7 % phi = N*N phase matrix for Kolmogorov turbulence
8
9 % find r0 for screen
10 k = 2*pi/lambda;
11 r0 = (0.423*k^2*Cn2*dz)^(-3/5);
12
13 % create discrete frequencies
14 del_f = 1/W; % frequency grid spacing [1/m]
15 fx = (-N/2 : N/2-1) * del_f;
16
17 % get magnitude from frequency components
18 [fx, fy] = meshgrid(fx);
19 [th, f] = cart2pol(fx, fy); % polar grid
20
21 % evaluate Kolmogorov power spectrum
22 Phi = 0.023*r0^(-5/3) .* f.^(-11/3);
23 Phi(N/2+1,N/2+1) = 0;
24

```

```

25 % random draws of Fourier coefficients
26 cn = (normrnd(0,1,N) + 1i*normrnd(0,1,N)) .* sqrt(Phi)*del_f; %
    ↪ synthesize the phase screen
27
28 % take inverse tranform to get phase
29 phi = real(ift2D(cn, 1));
30 end

```

```

1 function [phi, r0] = phase_screen_sh(Cn2, N, lambda, W, dz)
2 % Cn2 = local turbulence refractive structure parameter
3 % N = grid size of desired phase screen
4 % lambda = laser wavelength
5 % W = transverse window width
6 % dz = propagation distance
7 % phi = N*N phase matrix for Kolmogorov turbulence
8 %         (including subharmonics)
9 % r0 = plane wave Fried parameter
10
11 % find r0 for screen
12 k = 2*pi/lambda;
13 r0 = (0.423*k^2*Cn2*dz)^(-3/5);
14
15 % high-frequency phase contribution
16 phi_hi = phase_screen(Cn2, N, lambda, W, dz);
17
18 dx = W/(N-1);
19
20 % spatial grid [m]
21 [X, Y] = meshgrid((-N/2 : N/2-1) * dx);
22
23 % initialize low-freq screen
24 phi_lo = zeros(size(phi_hi));
25
26 % loop over low frequency grids with spacing 1/(3^p*W)
27 for p=1:3

```

```

28 % setup the PSD
29 del_f = 1 / (3^p*W); %frequency grid spacing [1/m]
30 fx = (-1 : 1) * del_f;
31 % frequency grid [1/m]
32 [fx , fy] = meshgrid(fx);
33 [th , f] = cart2pol(fx , fy); % polar grid
34
35 % evaluate Kolmogorov spectrum
36 Phi = 0.023*r0^(-5/3) .* f.^(-11/3);
37 Phi(2,2) = 0;
38
39 % random draws of Fourier coefficients
40 cn = (normrnd(0,1,3) + 1i*normrnd(0,1,3)).* sqrt(Phi)*del_f;
41 SH = zeros(N);
42 % loop over frequencies on this grid
43 for ii = 1:9
44     SH = SH + cn(ii) * exp(1i*2*pi*(fx(ii)*X+fy(ii)*Y));
45 end
46 phi_lo = phi_lo + SH; % accumulate subharmonics
47 end
48
49 phi_lo = real(phi_lo) - mean(real(phi_lo(:)));
50
51 % sum hi and low frequency contributions
52 phi = phi_lo + phi_hi;
53 end

```

APPENDIX B: Full MATLAB Propagation Code

The Full MATLAB propagation code is adapted from [14].

```
1 % Set up initial laser , target parameters
2 N = 512;%[256 256 512]; % bin number
3 P0 = 100e3; % output power [W]
4 a = [0.025 0.1 0.25]; % beam director radius [m]
5 Ws = 20*a; % window width in source plane [m]
6 W = [0.9 0.45 0.35]; % window width in target plane [m]
7 lambda = 1e-6; % wavelength [m]
8 c=3e8; % light speed [m/s]
9 eps0 = 8.85e-12; % vacuum permittivity [F/m]
10 % new parameters
11 rng (7); % seed random # generator
12 zsteps = 30; % number of turbulent phase screens
    % function properly calculate the r0pw
14 Cn2 = 1e-15*ones(1,zsteps);%linspace(1e-14,1e-15,zsteps); %
    ↪ refractive structure constant [m ^(-2/3)]
15 epsilon = linspace(1e-4,1e-4,zsteps); % extinction coefficient
    ↪ [1/ m]
16 f1 = 3000; % focal length [m]
17 k = 2*pi/lambda ; % wave number [m^-1]
18 realizations = 100; % # of realizations
19
20 % set up steps
21 z = linspace(0,f1,zsteps); % travel path
22 dz=z(end)/zsteps; % propagation distance , each step
23
24 % calculate fried parameter
25 r0 = FriedSpherical(lambda,Cn2,z);
26
27 % calculate theoretical spot size
```

```

28 Wd = 0.594*lambda*f1./(2*a);           % Spot radius diffraction
    ↪ contribution
29 Wt = (2*lambda*f1/(pi*r0));           % Spot radius turbulence
    ↪ contribution
30 W_tot_th = sqrt(Wd.^2 + Wt.^2);       % Overall spot radius (m)
31
32 % calculate theoretical peak intensity
33 Pz = BeerLambert(P0,epsilon,z);        % power at the target
34 I_peak_th = Pz./(pi*W_tot_th.^2);      % peak intensity at the target
35
36 w_tot = [];
37 I_peak = [];
38 figure
39 tiledlayout(1,3)
40 for i = 1:length(a)
    % window sizes along path
    Wz = linspace(Ws(i), W(i), zsteps+1);
43
44     % initial field at beam director
45     E0 = sqrt(2*P0/(c*epsilon*pi*a(i)^2));
46     [Xs, Ys, Es] = circ(Ws(i), a(i), N);
47     Es = E0*Es;
48
49     % focus onto target
50     phiBD = -k/(2*f1)*(Xs.^2 + Ys.^2);
51     Es = Es.*exp(1i*phiBD);
52
53     % Initialize irradiance array :
54     If = zeros(N);
55
56     % Iterate over realizations
57     for ir = 1:realizations
58
59         % Display the current iteration (it takes along time to
            ↪ finish !)

```

```

60    clc; disp (ir);
61
62    % Propagate from source to target
63    Ef=Es;
64    for iz = 1:zsteps
65        % create / apply turbulent phase screen
66        [phi, r0pw] = phase_screen_sh(Cn2(iz),N,lambda,Wz(iz)
67            ↪ ,dz);
68        Ef = Ef .* exp (1i*phi);
69
70        % % warn if step size too large
71        % if r0pw < 2*a(i)
72        %     disp (" More zsteps may be needed ");
73        % end
74
75        % diffraction ( replace Ef with each step )
76        [Ef,X,Y] = fresnel_conv (Ef,lambda ,Wz(iz) ,Wz(iz+1) ,
77            ↪ dz);
78    end
79
80    % Add irradiance of current realization
81    If = If + c* eps0 *abs (Ef) .^2/2;
82
83    % Get average irradiance profile
84    If = If/ realizations ;
85
86    % If an extinction coefficient is supplied , you can apply
87    % Beer 's law here :
88    If = BeerLambert(If , epsilon ,z);
89
90    % fing W_tot and time averaged peak intensity
91    [w_tot(end+1) , I_peak(end+1)] = fit_gaussian2D (If ,X);

```

```

92 function [r0] = FriedSpherical(lambda,Cn2,z)
93 % lambda = laser wavelength [m]
94 % Cn2 = 1D array of Cn2 values along z [m^(-2/3)]
95 % z = 1D array of corresponding positions along the beam path [m]
96 % r0 = spherical Fried parameter [m]
97 k = 2*pi/lambda; % wave number
98 R = z(end); % Target Distance
99 dist = (1-z/R).^(5/3); % distance contributor of the
    ↪ integrand
100 F = Cn2.*dist; % function to be integrated
101 r0 = (0.423*k^2*trapz(z,F))^(−3/5); % calculate Fried parameter
102 end
103
104 function [Pz] = BeerLambert(P0,epsilon,z)
105 % P0 = power at beam director [W]
106 % epsilon = 1D array of extinction coefficients along z [1/m]
107 % z = 1D array of corresponding z positions [m]
108 % Pz = attenuated power at z(end) [W]
109 Pz = P0*exp(−1*trapz(z,epsilon));
110 end
111
112 function [wtot, Ipeak] = fit_gaussian2D(I,X)
113 % I = 2D array of (time-averaged) intensity [W/m^2]
114 % X = 2D array of x-values for intensity array
115 % wtot = rms radius of Gaussian fit [m]
116 % Ipeak = peak of Gaussian fit [W/m^2]
117
118 N = size(I,1); % get grid size
119 mid = ceil(N/2); % find middle index of array
120
121 Ixmid = I(mid,:); % extract middle in x-direction
122 Iymid = I(:,mid); % extract middle in y-direction
123 Xmid = X(mid,:); % get x-values of middle row
124
125 % Gaussian fit in x-direction

```

```

126 coefx = fit(Xmid', Ixmid', 'gauss1', 'Robust', 'LAR');
127 coefx = coeffvalues(coefx); % 1st element = peak, 3rd element =
    ↪ standard deviation
128
129 % Gaussian fit in y-direction
130 coefy = fit(Xmid', Iymid, 'gauss1', 'Robust', 'LAR');
131 coefy = coeffvalues(coefy); % 1st element = peak, 3rd element =
    ↪ standard deviation
132
133 % get averages
134 wtot = (coefx(3) + coefy(3))/2;
135 Ipeak = (coefx(1) + coefy(1))/2;
136 end

```

THIS PAGE INTENTIONALLY LEFT BLANK

Disclosure of Generative AI Use in Supporting Writing

Professor Cohn, Professor Blau, and I agreed on the limited use of OpenAI's ChatGPT to improve grammar, punctuation, and conciseness in my thesis. For each paragraph, I requested ChatGPT to first identify and correct any spelling and grammar errors, then suggest improvements for clarity and conciseness. I specifically asked for the suggestions to be presented in a side-by-side table, comparing the original text with the recommended revisions. I reviewed each recommendation individually, and carefully considered all AI-generated suggestions before adopting them. For further quality control, I also consulted with Graduate Writing Center coaches.

THIS PAGE INTENTIONALLY LEFT BLANK

List of References

- [1] R. O'Rourke, "Navy shipboard lasers for surface, air, and missile defense," Congressional Research Service, Washington DC, USA, CRS Report No. R41526, 2015. [Online]. Available: <https://crsreports.congress.gov/product/details?prodcode=R41526>.
- [2] A. Kavvada, A. Ruiz-Barradas, and S. Nigam, "AMO's structure and climate footprint in observations and IPCC AR5 climate simulations," *Climate Dynamics*, vol. 41, no. 5, pp. 1345–1364, Sep. 2013. [Online]. Available: <https://doi.org/10.1007/s00382-013-1712-1>.
- [3] "Directed energy weapon," Wikipedia, Accessed: Apr. 17, 2024. [Online]. Available: https://en.wikipedia.org/wiki/Directed-energy_weapon.
- [4] D. H. Titterton, *Military Laser Technology and Systems*. Norwood, MA, USA: Artech House, 2015.
- [5] G. Perram, S. Cusumano, R. Hengehold, and S. Fiorino, *An Introduction to Laser Weapon Systems*. Dayton, OH, USA: Directed Energy Professional Society, 2010.
- [6] J. Jones, "Chemical lasers: Section introduction," in *Handbook of Laser Technology and Applications: Laser Design and Laser Systems*, C. Guo and S. C. Singh, Eds., 2nd ed. pp. 449, vol. 2, Boca Raton, FL, USA: CRC Press, 2021.
- [7] B. Barmashenko and S. Rosenwaks, "Chemical lasers: COIL," in *Handbook of Laser Technology and Applications: Laser Design and Laser Systems*, C. Guo and S. C. Singh, Eds., 2nd ed. pp. 451-465, vol. 2, Boca Raton, FL, USA: CRC Press, 2021.
- [8] L. H. Sentman, "Chemical lasers: HF/DF," in *Handbook of Laser Technology and Applications: Laser Design and Laser Systems*, C. Guo and S. C. Singh, Eds., 2nd ed. pp. 467-474, vol. 2, Boca Raton, FL, USA: CRC Press, 2021.
- [9] "Chemical laser," Electricity and Magnetism, Accessed: May 10, 2024. [Online]. Available: <https://www.electricity-magnetism.org/chemical-laser/>.
- [10] V. Antsiferov and G. Smirnov, *Physics of Solid State Lasers*. Cambridge, U.K.: Cambridge International Science Publishing, 2005. [Online]. Available: ProQuest.
- [11] "Solid-state laser," Electricity and Magnetism, Accessed: May 26, 2024. [Online]. Available: <https://www.electricity-magnetism.org/solid-state-laser/>.

- [12] L. R. Elias, “A Tutorial on Free-Electron Lasers,” in *Ninth International Symposium on Gas Flow and Chemical Lasers*, 1992. [Online]. Available: SPIE.
- [13] “Free-electron laser,” Electricity and Magnetism, Accessed: May 12, 2024. [Online]. Available: <https://www.electricity-magnetism.org/free-electron-laser/>.
- [14] J. Blau, “Directed energy weapons,” class notes for PH4858: Directed Energy Weapons, Dept. of Physics, Naval Postgraduate School, Monterey, CA, USA, Aut. 2024.
- [15] K. J. Kasunic, *Laser Systems Engineering*. Bellingham, WA, USA: SPIE, 2016. [Online]. Available: <https://doi.org/10.1117/3.2247601>.
- [16] S. Lower, *Geochemistry*. Simon Fraser University, British Columbia, Canada: LibreTexts Chemistry, 2024. [Online]. Available: LibreTexts.
- [17] F. G. Gebhardt, “High power laser propagation,” *Applied Optics*, vol. 15, no. 6, pp. 1479–1493, Jun. 1976. [Online]. Available: <https://doi.org/10.1364/AO.15.001479>.
- [18] P. Nielsen, *Effects of Directed Energy Weapons*. Washington, D.C., USA: NDU Press, 1994.
- [19] J. Tatum, *Planetary Photometry*. University of Victoria, British Columbia, Canada: LibreTexts Physics, 2024. [Online]. Available: LibreText.
- [20] C. Bardos and O. Pironneau, “The radiative transfer model for the greenhouse effect,” *SeMA Journal*, vol. 79, no. 3, pp. 489–525, Sep. 2022. [Online]. Available: <https://doi.org/10.1007/s40324-021-00265-y>.
- [21] D. L. Fried, “Optical resolution through a randomly inhomogeneous medium for very long and very short exposures,” *Journal of the Optical Society of America*, vol. 56, no. 10, pp. 1372–1379, 1966. [Online]. Available: <https://doi.org/10.1364/JOSA.56.001372>.
- [22] D. Smith, “High-power laser propagation: Thermal blooming,” *Proceedings of the IEEE*, vol. 65, no. 12, p. 1679, 1977. [Online]. Available: <https://doi.org/10.1109/PROC.1977.10809>.
- [23] R. G. Lane, A. Glindemann, and J. C. Dainty, “Simulation of a Kolmogorov phase screen,” *Waves in Random Media*, vol. 2, no. 3, pp. 209–224, 1992. [Online]. Available: <https://doi.org/10.1088/0959-7174/2/3/003>.
- [24] J. Blau, “High energy laser lethality,” class notes for PH4858: Directed Energy Weapons, Dept. of Physics, Naval Postgraduate School, Monterey, CA, USA, Aut. 2024.

- [25] P. J. Torvik, “Predictions of melt-through times for laser heating,” *AIAA Journal*, vol. 14, no. 4, pp. 417–418, 1976. [Online]. Available: <https://doi.org/10.2514/3.61379>.
- [26] P. J. Torvik, “Some further numerical studies of laser induced melting and vaporization,” Air Force Institute of Technology, Wright-Patterson Air Force Base, OH, USA, AFIT TR 73-1, 1973. [Online]. Available: <https://apps.dtic.mil/sti/citations/AD0760113>.
- [27] P. J. Torvik, “A numerical procedure for two dimensional heating and melting calculations, with applications to laser effects,” Air Force Institute of Technology, Wright-Patterson Air Force Base, OH, USA, AFIT TR 72-2, 1972. [Online]. Available: <https://apps.dtic.mil/sti/citations/AD0757189>.
- [28] P. A. Frederickson, “Integrating atmospheric optical turbulence and numerical weather prediction models for laser performance predictions,” in *SPIE Optical Engineering and Applications*, 2019. [Online]. Available: SPIE.
- [29] H. Hersbach, B. Bell, and P. Berrisford et al., “The ERA5 global reanalysis,” *Quarterly Journal of the Royal Meteorological Society*, vol. 146, no. 730, pp. 1999–2049, Jul. 2020. [Online]. Available: <https://doi.org/10.1002/qj.3803>.
- [30] “Material Properties Database,” Object name 7075-T6 Aluminum, Accessed: Jun. 6, 2024. [Online]. Available: <https://www.makeitfrom.com/material-properties/7075-T6-Aluminum/>.
- [31] “Material Properties Database,” Object name 304 Stainless Steel, Accessed: Jun. 6, 2024. [Online]. Available: <https://www.makeitfrom.com/material-properties/Grade-5-Ti-6Al-4V-3.7165-R56400-Titanium>.
- [32] “Material Properties Database,” Object name Grade 5 Titanium, Accessed: Jun. 6, 2024. [Online]. Available: <https://www.makeitfrom.com/material-properties/Grade-5-Ti-6Al-4V-3.7165-R56400-Titanium>.

THIS PAGE INTENTIONALLY LEFT BLANK

Initial Distribution List

1. Defense Technical Information Center
Ft. Belvoir, Virginia
2. Dudley Knox Library
Naval Postgraduate School
Monterey, California